

# Growing primordial continental crust self-consistently in global mantle convection models

Charitra Jain<sup>a,b</sup>, Antoine B. Rozel<sup>a</sup>, Paul J. Tackley<sup>a</sup>, Patrick Sanan<sup>a</sup>, Taras V. Gerya<sup>a</sup>

<sup>a</sup>*Institute of Geophysics, Department of Earth Sciences, ETH Zurich, Sonneggstrasse 5, CH-8092 Zurich, Switzerland*

<sup>b</sup>*now at Department of Earth Sciences, Durham University, Science Labs, Durham DH1 3LE, United Kingdom*

---

## Abstract

The majority of continental crust formed during the hotter Archean was composed of Tonalite-Trondhjemite-Granodiorite (TTG) rocks. In contrast to the present-day loci of crust formation around subduction zones and intra-plate tectonic settings, TTGs are formed when hydrated basalt melts at garnet-amphibolite, granulite or eclogite facies conditions. Generating continental crust requires a two step differentiation process. Basaltic magma is extracted from the pyrolytic mantle, is hydrated, and then partially melts to form continental crust. Here, we parameterise the melt production and melt extraction processes and show self-consistent generation of primordial continental crust using evolutionary thermochemical mantle convection models. To study the growth of TTG and the geodynamic regime of early Earth, we systematically vary the ratio of intrusive (plutonic) and eruptive (volcanic) magmatism, initial core temperature, and internal friction coefficient. As the amount of TTG that can be extracted from the basalt (or basalt-to-TTG production efficiency) is not known, we also test two different values in our simulations, thereby limiting TTG mass to 10% or 50% of basalt mass. For simulations with lower basalt-to-TTG production efficiency, the volume of TTG crust produced is in agreement with net crustal growth models but overall crustal (basaltic and TTG) composition stays more mafic than expected from geochemical data. With higher production efficiency, abundant TTG crust is produced, with a production rate far exceeding typical net crustal growth models but the felsic to mafic crustal ratio follows the expected trend. These modelling results indicate that (i) early Earth exhibited a “plutonic squishy lid” or vertical-tectonics geodynamic regime, (ii) present-day slab-driven subduction was not necessary for the production of early continental crust, and (iii) the Archean Earth was dominated by intrusive magmatism as opposed to “heat-pipe” eruptive magmatism.

*Keywords:*

Archean TTG, mantle convection, early Earth, melting, crustal production

---

## 1. Introduction

Floating at the top of the mantle and helping to sustain life, continents cover about a third of the Earth’s surface area. They have cores of Archean and Proterozoic cratonic basements

---

*Email addresses:* charitrajaingeo@gmail.com (Charitra Jain), antoine.rozel@erdw.ethz.ch (Antoine B. Rozel), paul.tackley@erdw.ethz.ch (Paul J. Tackley), patrick.sanan@erdw.ethz.ch (Patrick Sanan), taras.gerya@erdw.ethz.ch (Taras V. Gerya)

*Preprint submitted to Gondwana Research*

*May 10, 2019*

(Goodwin, 1991; Hoffmann, 1989) underlying a chemically evolved continental crust. With an average thickness of  $34.4 \pm 4.1$  km (Huang et al., 2013), continental crust is separated from the ultramafic rocks of the mantle by the Mohorovičić discontinuity. Compared to the thin (7 km on average) and ephemeral oceanic crust with a maximum life span of  $\sim 200$  million years, continental crust is much older (Rudnick and Gao, 2003). The crust is andesitic in composition, which lies between basalt and rhyolite with 60.6% SiO<sub>2</sub> and 4.7% MgO (Hawkesworth and Kemp, 2006a). Though accounting for only 0.57% of the mass of the Earth's mantle, continental crust is significantly richer in incompatible trace elements and acts as a geochemical repository (Hofmann, 1988).

Two stages of differentiation are generally inferred to generate continental crust. First, basaltic magma is extracted from the mantle. Second, it is buried and partially melts to form more silicic continental crust with the possible help of sedimentary processes (e.g., Rudnick, 1995; Rudnick and Gao, 2003; Taylor and McLennan, 1985; Albarède, 1998; Arculus, 1999; Kemp and Hawkesworth, 2003; Plank, 2005; Hawkesworth and Kemp, 2006b). Considering that a basaltic precursor is needed for its generation, continental crust has long been assumed to form in only two distinct plate tectonic settings (Rudnick, 1995). Either the basaltic protolith is sourced from convergent plate margins at island or continental arcs where oceanic crust subducts, or it originates from an intra-plate tectonic setting as a result of plume-associated magmatism or extensional tectonics. For present day continental crust, the dominant role of island arc basalts (IAB: present-day representative of subduction magmas) over ocean island basalts (OIB: present-day representative of intra-plate magmas) has been highlighted (Taylor and McLennan, 1985; Sun and McDonough, 1989; Rudnick, 1995; Arculus, 1999; Barth et al., 2000; Hawkesworth and Kemp, 2006b).

However, during the Archean Eon (4.0-2.5 Ga), the upper mantle potential temperature is estimated to be  $\sim 250$  K higher than its present-day value (Labrosse and Jaupart, 2007; Herzberg and Gazel, 2009; Herzberg et al., 2010; Condie et al., 2016). A large proportion of Archean continental crust is made of grey gneiss complexes, among which a group of sodic granitoids collectively known as Tonalite-Trondhjemite-Granodiorite (TTG) is the main lithological component (Jahn et al., 1981; Drummond and Defant, 1990; Martin, 1994). Based on experimental data, it is suggested that Archean TTGs are formed when hydrated basalt melts at garnet-amphibolite, granulite or eclogite facies conditions (e.g., Barker and Arth, 1976; Jahn et al., 1981; Rapp et al., 1991; Condie, 1986; Martin, 1986; Springer and Seck, 1997; Foley et al., 2002; Rapp et al., 2003; Moyen and Stevens, 2006). Sourced from similar compositions but melted over a range of pressures, Archean TTGs are classified by Moyen (2011) into three different types: low, medium, and high pressure TTGs. Furthermore, the low-pressure (10-12 kbar), medium-pressure (ca. 15 kbar) and high-pressure (20 kbar or higher) groups account for 20%, 60% and 20% of the sodic TTGs respectively. Specific pressure-temperature conditions corresponding to different tectonic settings for these TTG types are proposed by Moyen (2011) and these are used as a criterion for generating Archean TTG in our geodynamic models.

In a recent review on continental growth, Dhuime et al. (2017) proposed that 65% of the present continental crust existed before 3 Ga. This is supported with similar results from different continental growth models built on records of detrital zircons and sedimentary rocks. Moreover, it is argued that there has been a continuous growth of continental crust over the evolution of the planet with a significant drop in average net growth rate from  $2.9 - 3.4 \text{ km}^3 \text{ yr}^{-1}$  to  $0.6 - 0.7 \text{ km}^3 \text{ yr}^{-1}$  around  $\sim 3$  Ga. Interestingly, it is suggested that Earth might have undergone a major tectonic regime transition around the same time owing to secular cooling and the resulting evolution of mantle viscosity (e.g., van Hunen et al., 2008; Sizova et al., 2010; Van Kranendonk,

2010; Korenaga, 2011, 2013; van Hunen and Moyen, 2012; Debaille et al., 2013; Gerya, 2014; Johnson et al., 2013a, 2017; Gerya et al., 2015; Condie et al., 2016; Fischer and Gerya, 2016; Van Kranendonk and Kirkland, 2016; Rozel et al., 2017). Based on geochemical data, Tang et al. (2016) suggested that this global geodynamic transition marks the period of significant silicification of the continental crust, which could be explained by the peeling off and recycling of the mafic lower continental crust after the onset of Archean-style plate tectonics (Chowdhury et al., 2017).

The answer to the question of when plate tectonics commenced on Earth remains hotly debated, with a multitude of studies proposing its inception anytime between the Hadean Eon (4.5-4.0 Ga) and the Neoproterozoic Era (1.0-0.54 Ga) (see Korenaga (2013); Dhuime et al. (2017) and the references within). The igneous zircons from Jack Hills, Western Australia that formed > 4 billion years ago make up for a sparse geological record of the early Earth (Wilde et al., 2001). Hopkins et al. (2008, 2010) proposed that these zircons formed in environments that are similar to modern convergent margins. It is therefore argued that plate tectonics might have been active during the Hadean Eon (4.5-4.0 Ga). Many authors prefer the Archean Eon (4.0-2.5 Ga) for the onset of plate tectonics because relevant indicators, such as orogens, accretionary prisms, and paired metamorphic belts became more prevalent in the late Archean (e.g., Komiya et al., 1999; Brown, 2006; Van Kranendonk et al., 2007; Shirey et al., 2008; Condie and Kröner, 2008). Citing the lack of ultrahigh-pressure metamorphism and ophiolites before the Neoproterozoic Era (1.0-0.54 Ga), Stern (2005) argued that plate tectonics could not have been operational before 1 Ga. Some studies attributed the aforementioned decline in growth of continental crust to higher crustal recycling and the onset of subduction-driven plate tectonics around ~ 3 Ga (e.g., Cawood et al., 2006; Shirey and Richardson, 2011; Dhuime et al., 2012; Hawkesworth et al., 2016, 2017).

The formation of Archean TTGs and the enigma behind the origin of plate tectonics have piqued the interest of the geodynamics community over the years. About a decade and a half ago, by using thermo-chemical mantle convection models, van Thienen et al. (2004) proposed that the transition of basalt into denser eclogite at a depth of 30 km creates a gravitational instability. This might trigger a resurfacing event in which a major portion of the crust sinks into the mantle and the resulting pressure release melting produces new replacement crust. In these models, the felsic melts are generated by partial melting either at the base of this new crust or when the dense crust sinks into the mantle. Moore and Webb (2014) offered an alternative scenario for early Earth, in which volcanism dominates the surface heat transport (heat-pipe Earth). Erupting all the mafic melt at the surface creates a cold and thick lithosphere (O'Reilly and Davies, 1981). This thickened lithosphere is advected downward and may melt to generate felsic volcanics and TTG plutons.

However, neither of these models considered generating and emplacing the felsic melts within or beneath the crust. Geological field data suggests that the majority of mantle-derived melts intrude at depth, with the ratio of intrusive (plutonic) to eruptive (volcanic) melt volumes ranging between 4:1 and 10:1 (Crisp, 1984). This would correspond to an eruption efficiency between 9% and 20%. Using sophisticated coupled petrological-thermomechanical regional-scale numerical experiments, Sizova et al. (2015) identified three distinct tectono-magmatic settings in which felsic melts can be generated from hydrated basaltic crust in the hotter Archean conditions. Lower crustal delamination and the subsequent dripping or small-scale overturns could generate Archean TTGs whereas the rest of the Archean granitoids could come from local thickening of primitive basaltic crust.

Rozel et al. (2017) have recently demonstrated the possibility of tracking formation condi-

Table 1: Non-dimensional and dimensional parameters along with the rheological properties for 3 different layers  $i$  used in this study (UM = Upper Mantle (dry olivine); PV = Perovskite; PPV = Post-Perovskite)

Property	Symbol	Value	Units
Rayleigh number	$Ra$	$7.73 \cdot 10^7$	-
Initial internal heating rate	$H$	$18.77 \cdot 10^{-12}$	W/kg
Half-life	$t_{\text{half}}$	2.43	Gyr
Surface ductile yield stress	$\sigma_y^d$	40	MPa
Ductile yield stress gradient	$\sigma_y^d'$	0.01	-
Reference viscosity	$\eta_0$	$1 \cdot 10^{21}$	Pa·s
Surface temperature	$T_{\text{surf}}$	300	K
Initial potential temperature	$T_{p0}$	1900	K
Gas constant	$R$	8.3145	J/K/mol
Gravity	$g$	9.81	m/s <sup>2</sup>
Mantle thickness	$D$	2890	km
Specific heat capacity of pyrolite	$C_{p,\text{pyr}}$	1200	J/kg/K
Specific heat capacity of basalt	$C_{p,\text{bas}}$	1000	J/kg/K
Specific heat capacity of TTG <sup>c</sup>	$C_{p,\text{TTG}}$	1000	J/kg/K
Latent heat of pyrolite	$L_{\text{pyr}}$	600	kJ/kg
Latent heat of basalt	$L_{\text{bas}}$	380	kJ/kg
Latent heat of TTG <sup>d</sup>	$L_{\text{TTG}}$	300	kJ/kg
Surface thermal expansivity <sup>e</sup>	$\alpha$	$3 \cdot 10^{-5}$	K <sup>-1</sup>
Surface thermal conductivity <sup>f</sup>	$k$	3.5	W/m/K
Activation energy - UM	$E_1$	300	kJ/mol
Activation volume - UM	$V_1$	5.00	cm <sup>3</sup> /mol
Pressure scale - UM	$P_1$	$\infty$	GPa
Viscosity multiplier - UM	$\Delta\eta_1$	1.0	-
Activation energy - PV	$E_2$	370	kJ/mol
Activation volume - PV	$V_2$	3.65	cm <sup>3</sup> /mol
Pressure scale - PV	$P_2$	200	GPa
Viscosity multiplier - PV	$\Delta\eta_2$	30.0	-
Activation energy - PPV	$E_3$	162	kJ/mol
Activation volume - PPV	$V_3$	1.40	cm <sup>3</sup> /mol
Pressure scale - PPV	$P_3$	1610	GPa
Viscosity multiplier - PPV	$\Delta\eta_3$	0.1	-

<sup>c</sup> 1200 J/kg/K for simulations presented in Table 4

<sup>d</sup> 600 kJ/kg for simulations presented in Table 4

<sup>e</sup> valid at the surface for olivine phase system.

tions for Archean TTGs in numerical simulations on a global scale, which motivated our numerical modelling study. Their study showed that a plutonism-dominated plutonic squishy lid tectonic regime results in hotter crustal geotherms and is able to reproduce the observed proportions of various TTG rocks, as reported by Moyen (2011). Here, we present global mantle convection simulations in which continental crust is generated self-consistently. Based on the melting conditions proposed by Moyen (2011), we parameterise TTG formation and investigate continental growth and recycling by systematically varying parameters such as eruption efficiency, basalt-to-TTG production efficiency, initial core temperature, and friction coefficient. We introduce the methodology with a focus on melting parameterisation in section 2. We present the results of our simulations in section 3 and discuss their geophysical implications in section 4. Finally, we summarise the main findings of our study in section 5.

## 2. Physical Model and Numerical Model

We model the thermo-chemical evolution of the compressible mantle using the code StagYY (Tackley, 2008), which has been extended by implementing a new two-stage crustal growth algorithm needed for our study. The models incorporate pressure- and temperature-dependence of viscosity, plasticity, internal and basal heating, core cooling, phase transitions, and melting leading to both basaltic and TTG crust production. The values used for the parameters are given in Table 1.

## 2.1. Rheology

Diffusion creep with homogenous grain size is considered as the viscous deformation mechanism. The mantle has 3 different layers  $i$ : upper mantle (1), lower mantle (2) and post-perovskite layer (3), with each layer having different values for activation energy  $E_i$  and activation volume  $V_i$  (Karato and Wu, 1993; Yamazaki and Karato, 2001). The temperature- and pressure-dependent viscosity  $\eta$  in each layer follows the Arrhenius formulation (see Table 1 for constants):

$$\eta(T, P) = \eta_0 \Delta\eta_i \exp\left(\frac{E_i + PV_i}{RT} - \frac{E_i}{RT_0}\right), \quad (1)$$

where  $\eta_0$  is the reference viscosity at zero pressure and reference temperature  $T_0$  (1600 K),  $\Delta\eta_i$  is the viscosity offset between layer  $i$  and the reference viscosity (corresponding to material between the phase transitions, see Section 2.3),  $P$  is the pressure,  $R$  is the gas constant and  $T$  is the absolute temperature.  $\eta_0$  is valid for the phase system olivine and the reference composition (60% olivine and 40% pyroxene-garnet), both of which have viscosity multipliers of 1 (see Table 1). The activation volume decreases exponentially with increasing pressure in each layer  $i$  according to the relation:

$$V(P) = V_i \exp\left(-\frac{P}{P_i}\right). \quad (2)$$

where  $P_i$  is the pressure scale which is different for each layer  $i$  as given in Table 1. A viscosity jump of 30 is applied at the upper-lower mantle transition (600 km) in accordance with the viscosity profile expected by the inversion of postglacial rebound data (Čížková et al., 2012) and geoid inversion studies (e.g., Ricard et al., 1989, 1993). An additional viscosity jump of 0.1 (compared to reference viscosity) is imposed at the transition to post-perovskite at lowermost mantle depths (2740 km) following mineral physics experiments and theoretical calculations by Hunt et al. (2009); Ammann et al. (2010).

To allow for lithospheric deformation, plastic yielding is assumed to be the weakening mechanism (Moresi and Solomatov, 1998; Tackley, 2000). The maximum stress that a material can sustain before deforming plastically is given by the yield stress  $\sigma_Y$ , which has both brittle and ductile components:

$$\sigma_Y = \min(\sigma_{Y,ductile}, \sigma_{Y,brittle}). \quad (3)$$

The ductile yield stress  $\sigma_{Y,ductile}$  increases linearly with pressure as:

$$\sigma_{Y,ductile} = \sigma_Y^0 + \sigma'_Y P, \quad (4)$$

where  $\sigma_Y^0$  is the surface ductile yield stress and  $\sigma'_Y$  is the pressure gradient of the ductile yield stress. Following Byerlee (1978), the brittle yield stress  $\sigma_{Y,brittle}$  is calculated as

$$\sigma_{Y,brittle} = \mu P, \quad (5)$$

where  $\mu$  is the friction coefficient. Different values of the friction coefficient for the lithosphere that are consistent with experimentally-measured values are used in this study. If the convective stresses exceed the yield stress, the viscosity is reduced to the yielding viscosity  $\eta_Y = \sigma_Y/2\dot{\epsilon}$ , where  $\dot{\epsilon}$  is the 2nd invariant of the strain-rate tensor. The effective viscosity is then given by

$$\eta_{\text{eff}} = \left(\frac{1}{\eta} + \frac{2\dot{\epsilon}}{\sigma_Y}\right)^{-1}. \quad (6)$$

Viscosity limiters ( $10^{18}$  and  $10^{28}$  Pa-s) are then used to mitigate large viscosity variations, which would decrease the stability of the code.

## 2.2. Boundary Conditions and Solution Method

We solve the following equations for compressible anelastic Stokes flow with infinite Prandtl number:

$$\nabla \cdot (\rho \mathbf{u}) = 0, \quad (7)$$

$$\mathbf{0} = -\nabla P + \nabla \cdot \boldsymbol{\tau} + \rho \mathbf{g}, \quad (8)$$

$$\rho C_p \left( \frac{\partial T}{\partial t} + \mathbf{u} \cdot \nabla T \right) - \alpha T (u_r \cdot \nabla_r P) = \nabla \cdot (k \nabla T) + \boldsymbol{\tau} : \nabla \mathbf{u} + \rho H, \quad (9)$$

with density  $\rho$ , time  $t$ , velocity  $\mathbf{u}$ , gravity  $\mathbf{g}$ , heat capacity  $C_p$ , thermal expansivity  $\alpha$ , thermal conductivity  $k$ , deviatoric stress tensor  $\boldsymbol{\tau}$ , and  $H$  is the internal heating rate per unit mass.  $\boldsymbol{\tau} : \nabla \mathbf{u}$  denotes tensor contraction, such that:  $\boldsymbol{\tau} : \nabla \mathbf{u} = \sum_{ij} \tau_{ij} \partial v_i / \partial x_j$ , where  $x_j$  is the position. The values of the parameters used in this study are listed in Table 1.

We use 2D spherical annulus geometry (Hernlund and Tackley, 2008) with a resolution that varies radially and is higher at the surface, around the 660 km phase transition, and the core-mantle boundary. The computational domain consists of 1024 (laterally) times 128 (radially) cells. 3,932,160 tracers are advected through the mesh using a fourth-order Runge-Kutta scheme with a second-order spatial interpolation of the velocity field. This represents an initial average of 30 tracers per cell. However, during eruptive magmatism, an empty space is created in the surface cells by compacting the existing tracers radially inwards. The surface cells are then replenished with new tracers while a tracer merging algorithm tries to merge tracers to have a certain target mass. Each tracer carries several quantities such as temperature, composition, water content, concentration of heat-producing element, emplacement, and depletion. The tracer-to-cell interpolation is done following the tracer-ratio method as described by Tackley and King (2003), adapted to perform mass averaging of tracer quantities. We employ free-slip boundary conditions at the surface and the core-mantle boundary, which are also isothermal. The surface temperature is fixed at 300 K, while the core temperature decreases with time due to heat lost, using a parameterisation based on Buffett et al. (1992, 1996), for details of which the reader is referred to Nakagawa and Tackley (2004). A parallel MUMPS solver (Amestoy et al., 2000) used via an interface from the PETSc package (Balay et al., 2018a,b) is used to obtain a velocity-pressure solution at each time-step on a staggered grid.

## 2.3. Phase Changes and Composition

The model includes a parameterisation based on mineral physics data (Irifune and Ringwood, 1993; Ono et al., 2001), in which the minerals are divided into olivine, pyroxene-garnet, TTG and melt phase systems. Within the olivine and pyroxene-garnet phase systems we assume the solid-solid phase transitions as considered previously in Xie and Tackley (2004b); Nakagawa and Tackley (2012). The mixture of minerals depends on the composition, which is mapped linearly into the fraction of different phase systems. Composition can either be in the continuum between *harzburgite* (ultramafic and depleted material) and *basalt* (mafic igneous rocks), or *TTG* (felsic rocks) as shown in Fig. 1. Harzburgite is considered to be a mixture of 75% olivine and 25%

pyroxene-garnet and basalt is made of pure pyroxene-garnet. The mantle is initialised with a pyrolytic composition: 80% harzburgite and 20% basalt (Xu et al., 2008). At a depth of 60 km, basalt transforms to eclogite, which is around  $190 \text{ kg/m}^3$  denser than olivine. At lowermost mantle depths, the phase transition to post-perovskite is also considered (e.g. Tackley et al. (2013)). Additionally, TTG material undergoes coesite to stishovite phase transition as its density increases by  $168 \text{ kg/m}^3$  at a depth of 290 km (Akimoto and Syono, 1969; Akaogi and Navrotsky, 1984; Gerya et al., 2004; Ono et al., 2017). The phase change parameters are given in Table 2. Changes in composition arise from melt-induced differentiation, which is described in the next section.

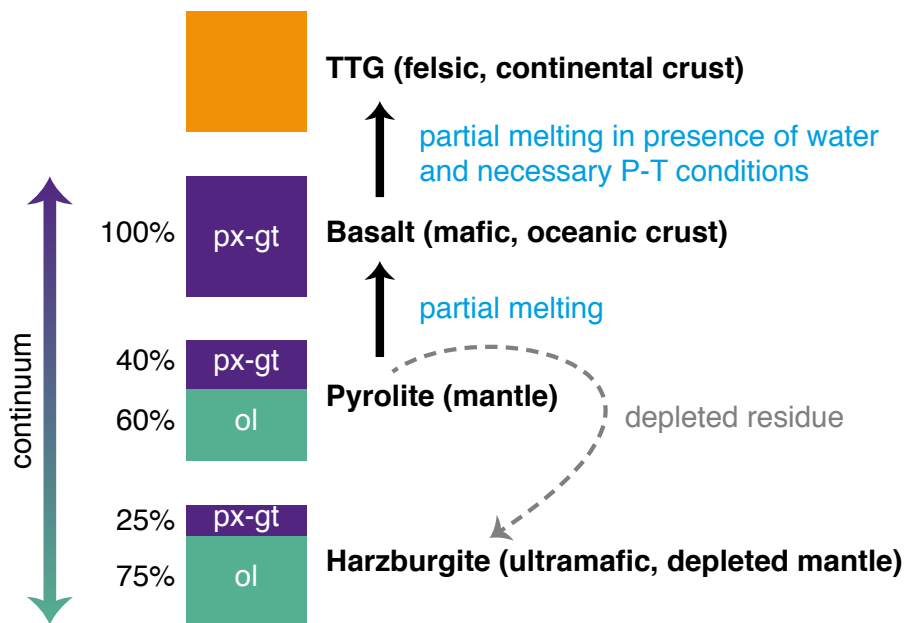


Figure 1: A one-dimensional compositional variation corresponding to variation of  $\text{SiO}_2$  content. Compositions in the continuous range basalt to harzburgite consist of a mixture of olivine (ol) and pyroxene-garnet (px-gt) mineralogies in different proportions.

#### 2.4. Melting and Crustal Production

For self-consistent creation of basaltic (mafic, oceanic-like) and TTG (felsic, continental-like) crust, we parameterise the processes of melt generation and melt extraction. For the sake of numerical efficiency, we compute the melt production at the cell level (with an average area of  $\sim 680 \text{ km}^2$ ). Molten tracers are then generated accordingly and transported upwards to erupt on or intrude into the pre-existing crust (mimicking large-scale eruptive and intrusive magmatism) if the appropriate conditions outlined in Section 2.4.1 are met. The model developed in this study is an extension of the ones previously described by Xie and Tackley (2004b); Nakagawa et al. (2010). Water tracking has been added, as water is essential for the production of TTG crust. Water is considered to penetrate fully into the top 10 km and is advected throughout the mantle on tracers. The non-dimensional water concentration varies between 1 implying fully hydrated and

Table 2: Phase change parameters for olivine, pyroxene-garnet, and TTG systems with surface density at zero pressure  $\rho_s$ , density jump across a phase transition  $\Delta\rho$ , and Clapeyron slope  $\gamma$ .

Depth (km)	Temperature (K)	$\Delta\rho$ (kg/m <sup>3</sup> )	$\gamma$ (MPa/K)
Olivine ( $\rho_s = 3240$ kg/m <sup>3</sup> )			
410	1600	180	2.5
660	1900	400	-2.5
2740	2300	61.6	10
Pyroxene-Garnet ( $\rho_s = 3080$ kg/m <sup>3</sup> )			
60	1000	350	0
400	1600	150	1
720	1900	400	1
2740	2300	61.6	10
TTG ( $\rho_s = 2700$ kg/m <sup>3</sup> )			
290 <sup>a</sup>	1713	168	2.26

<sup>a</sup> coesite-stishovite phase transition considered only for simulations presented in Table 3

0 meaning no water (see Fig. A.13A in Appendix) and is the same in both solid and melt phases (using partition coefficient  $D_{\text{part,H}_2\text{O}} = 1$ ). Heat-producing elements (HPE) are partitioned during melting and their non-dimensional concentration  $Rh^*$  is 100 times higher in the melt compared to the solid residue (using partition coefficient  $D_{\text{part,HPE}} = 0.01$ ; see Fig. A.13B in Appendix). A detailed description of our new melting-induced crustal production (MCP) procedure is given in the next sections.

#### 2.4.1. Melt generation

##### *Amount of melt produced*

As melting is calculated at the cell level, the cell-based solid composition  $C$  and melt fraction  $f$  have to be computed at cell centres using mass averaging of the tracers in each cell. At each time-step, the amount of melt  $\Delta f$  appearing in each cell is computed iteratively. More precisely, the cell temperature  $T$  is compared to the solidus  $T_{\text{sol},i}$  of each composition  $i$  giving individual changes in melt fraction  $\Delta f_i$ . In case the cell temperature exceeds or is lower than a composition's solidus, then melt is respectively generated or frozen (if already present) from that composition, with the goal of bringing the temperature back to the solidus. Latent heat  $L$  (see Table 1) of melt is consumed during melting and released during freezing and the resulting change in temperature  $\Delta T$  is computed for each cell. This is compared to the change in temperature  $DT$  needed to return the cell temperature to the solidus, and if not close enough, the procedure is iterated on. In principle, melting or solidification should occur at constant temperature (except for the slight change of melting temperature with composition). But as latent heat is absent from the heat equation, the process of latent heat related heating or cooling has to be done during the melting treatment as a correction. Effectively, due to compositional heterogeneities, different materials within each cell melt at different temperatures.

For simplicity, we consider 3 solidus temperatures (given in Fig. 2 and Appendix B):

- $T_{\text{sol,bas}}$  for pure basalt that has already been erupted or intruded,
- $T_{\text{sol,TTG}}$  for pure TTG,
- $T_{\text{sol,pyr}}$  for a harzburgite-basalt mixture or pure basalt that has never been erupted or intruded (see next section for details).

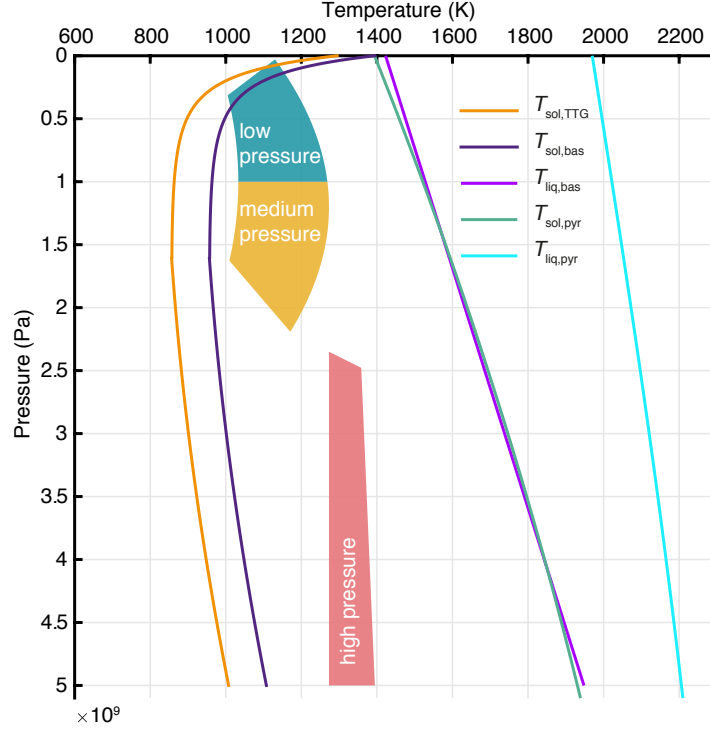


Figure 2: Solidi and liquidus used in this study for 3 different compositions: TTG, basalt, and pyrolite. Also visualised are the P-T conditions for 3 different types of TTGs as given in Eq. C.1, C.3 and taken from Moyen (2011).

The pyrolite solidus  $T_{\text{sol,pyr}}$  is adapted by the average composition in the cell to give the instantaneous melting temperature  $T_{\text{melting}}$  as:

$$T_{\text{melting}} = T_{\text{bas-out}} + (T_{\text{sol,pyr}} - T_{\text{bas-out}}) \min\left(\frac{C_{\text{bas}}}{C_{\text{ref-bas}}}, 2\right) \quad (10)$$

$$+ (T_{\text{liq,pyr}} - T_{\text{bas-out}}) \left(\frac{f_{\text{harz}}}{1 - C_{\text{ref-bas}}}\right), \quad (11)$$

with pyrolite liquidus  $T_{\text{liq,pyr}}$ , basalt fraction in the solid  $C_{\text{bas}}$ , reference basalt fraction in the solid  $C_{\text{ref-bas}} = 0.2$ , and fraction of harzburgite in the melt  $f_{\text{harz}}$ .  $T_{\text{bas-out}}$  is calculated as:

$$T_{\text{bas-out}} = T_{\text{sol,pyr}} + C_{\text{ref-bas}} (T_{\text{liq,pyr}} - T_{\text{sol,pyr}}). \quad (12)$$

The instantaneous melting temperature  $T_{\text{melting}}$  increases linearly with melt fraction  $f$  from 0 to  $T_{\text{basalt-out}}$ . Once basalt is exhausted,  $T_{\text{melting}}$  increases linearly with harzburgite fraction in the melt  $f_{\text{harz}}$  up to  $T_{\text{liq,pyr}}$ . As shown above, the instantaneous melting temperature  $T_{\text{melting}}$  is composition-dependent, and therefore depends on the amount of melt being produced. Hence, computing the variation of melt fraction in a cell for mantle material in the harzburgite-basalt continuum is difficult. In this case, a first order extrapolation of this melting temperature in the

melt fraction space is considered:

$$T_{\text{melting}}(f_0 + \Delta f) = T_{\text{melting}}(f_0) + \Delta f \left. \frac{\partial T_{\text{melting}}}{\partial f} \right|_{f_0}, \quad (13)$$

where  $f_0$  is the initial (basaltic/harzburgitic) melt fraction in the cell. The composition-dependence of the melting temperature  $\partial T_{\text{melting}}/\partial f$  is estimated by imposing a very small  $\Delta f$ . Using Eq. 13, the variation of melt fraction is then computed implicitly and iteratively using:

$$\Delta f = \frac{T - T_{\text{melting}}(f_0 + \Delta f)}{L} C_{P,\text{pyr}} = \frac{T - \left( T_{\text{melting}} + \Delta f \frac{\partial T_{\text{melting}}}{\partial f} \right)}{L} C_{P,\text{pyr}}, \quad (14)$$

where  $C_{P,\text{pyr}}$  is the specific heat capacity. Rearranging Eq. 14 and assuming that the solidus temperatures for basalt and TTG melting are not composition-dependent (i.e.,  $\partial T_{\text{sol,bas}}/\partial f = \partial T_{\text{sol,TTG}}/\partial f = 0$ ), we get:

$$\Delta f = \begin{cases} (T - T_{\text{melting}}) / \left( \frac{L_{\text{pyr}}}{C_{P,\text{pyr}}} + \frac{\partial T_{\text{melting}}}{\partial f} \right), & \text{for the mantle} \\ (T - T_{\text{sol,bas}}) C_{P,\text{bas}} / L_{\text{bas}}, & \text{for basalt} \\ (T - T_{\text{sol,TTG}}) C_{P,\text{TTG}} / L_{\text{TTG}}, & \text{for TTG} \end{cases}, \quad (15)$$

with latent heat of pyrolite  $L_{\text{pyr}}$ , specific heat capacity of pyrolite  $C_{P,\text{pyr}}$ , latent heat of basalt  $L_{\text{bas}}$ , specific heat capacity of basalt  $C_{P,\text{bas}}$ , latent heat of TTG  $L_{\text{TTG}}$ , and specific heat capacity of TTG  $C_{P,\text{TTG}}$ . TTG solidus is considered to be 100 K lower than the basalt solidus.

New melt fractions are obtained by adding the  $\Delta f_i$  of each composition  $i$  to its initial melt fraction  $f_i$ . New tracers of composition corresponding to  $\Delta f_i$  appear. The cell temperature is adjusted using the latent heat consumed through the generation of  $\Delta f_i$ .

#### Type of melt produced

The composition of the melts produced is obtained using the following procedure:

- Basaltic melt is produced using the instantaneous melting temperature  $T_{\text{melting}}$  when melting occurs on solid tracers with a mixed harzburgite-basalt composition (as in the beginning of the simulations). Pure basaltic solid tracers that have never been erupted or intruded also produce molten basalt using  $T_{\text{melting}}$ . This choice is motivated by the fact that non-erupted-intruded basaltic tracers represent basalt that is not a separate rock type, but rather a chemical component of rocks that are a chemical mixture of basaltic and harzburgitic end-member components, such as peridotite or pyrolite.
- When melting happens on a basaltic solid tracer that has been erupted or intruded in the past (hereafter, referred to as *solid-basalt* tracer), we consider it as a separate rock type. We therefore use the solidus temperature for pure basalt  $T_{\text{sol,bas}}$ . Depending on whether the cell satisfies the specific P-T conditions for TTG formation outlined by Moyen (2011) or not (see Appendix C), solid basalt can melt in two different ways. When the cell undergoes melting but it does not have TTG formation conditions, then basaltic melt is generated. Only when the cell has water (50% or more of the imposed surface hydration conditions) and *enriched basalt* (see section 2.4.2 for explanation), and meets the TTG formation conditions, is TTG melt generated.

- For simplicity, molten TTG is always produced when solid TTG melts, using the solidus temperature  $T_{\text{sol,TTG}}$ .
- Molten harzburgite (i.e., ultramafic melt) is produced in extreme cases (at the beginning of the simulations) when the entire basaltic mantle component is already molten and the cell temperature still exceeds the  $T_{\text{melting}}$  for harzburgite (see Appendix B).
- Basaltic crust that is older than 10 million years is also allowed to melt and erupt again as basalt, however it cannot be intruded as this material is already in the crust. We would have to intrude it where it already is, or even below its current depth.

The mantle is initially pyrolytic, with a composition corresponding to 20% basalt and 80% harzburgite end-member components. For partially-melting pyrolite to generate basalt, a solidus function fitting experimental data by Hirschmann (2000) is used (see Fig. 2 and Appendix B.2). For partially-melting basalt to generate TTG, the pressure-dependent solidus and liquidus functions are taken from Table 1 of Sizova et al. (2015) for “hydrated basalt” composition (as defined in their paper, see Fig. 2 and Appendix B.1.1). To simulate melt extraction from partially molten lithologies (Nikolaeva et al., 2008; Sizova et al., 2015), we do not allow the melting of all the basalt available in the mantle to generate TTG.

#### 2.4.2. Depletion fraction

When initialised, the entire mass of basalt on the *solid-basalt* tracer can potentially partially melt to form TTG (or *enriched basalt*). With each subsequent melting event, the proportion of *enriched basalt* available on the tracer decreases. Conversely, there is an increase in the proportion of *depleted basalt*, or the basalt that cannot melt to form TTG. The production of TTG from basalt is limited by introducing a parameter called depletion fraction  $X_{\text{depletion}}$ , which gives the allowable mass fraction of depleted basalt on a *solid-basalt* tracer. For example,  $X_{\text{depletion}} = 0.9$  implies that 90% of basalt is depleted or not available for TTG production. Hence, only 10% of mass of *solid-basalt* will be used for TTG production (basalt-to-TTG production efficiency). This is an important parameter as it directly controls how much felsic crust can be produced in a simulation.

The amount of TTG melt to be generated by the melting of *solid-basalt* is given by  $\Delta f_{\text{basalt-to-TTG}}$ . Using this, the ideal amount of TTG to be generated in a cell with mass  $M_{\text{cell}}$  is given as:

$$\Delta M_{\text{TTG}} = \Delta f_{\text{basalt-to-TTG}} M_{\text{cell}}. \quad (16)$$

This amount has to be sourced uniformly from the *solid-basalt* tracers present in the cell:

$$\Delta M_{\text{TTG}} = \sum_{i=1}^{n \text{ tracers}} \Delta m_{\text{TTG},i}, \quad (17)$$

where  $\Delta m_{\text{TTG}}$  is the mass of TTG produced from the host tracer  $i$ . *Solid-basalt* tracers are 100% enriched in basalt at time  $t = 0$  and after a time step  $\Delta t$ , the new amount of *enriched basalt* on a tracer is:

$$m_{\text{enr},i}(t + \Delta t) = m_{\text{enr},i}(t) - \Delta m_{\text{dep},i} - \Delta m_{\text{TTG},i}, \quad (18)$$

where  $m_{\text{enr}}$  and  $m_{\text{dep}}$  denote the masses of *enriched basalt* and *depleted basalt* on the tracer, respectively (see Fig. 3 for illustration). The change in masses of *depleted basalt*  $\Delta m_{\text{dep}}$  and TTG

$\Delta m_{\text{TTG}}$  (produced from *enriched basalt*) are related using the depletion fraction  $X_{\text{depletion}}$  as

$$\Delta m_{\text{dep},i} = \Delta m_{\text{TTG},i} \left( \frac{X_{\text{depletion}}}{1 - X_{\text{depletion}}} \right). \quad (19)$$

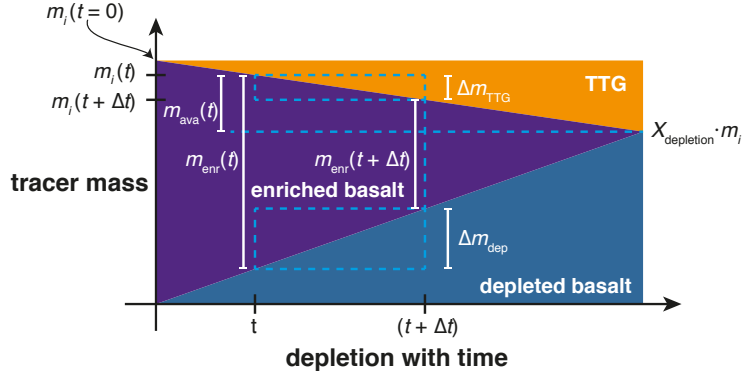


Figure 3: Evolution of depletion on a *solid-basalt* tracer with time. The initial tracer mass  $m_i$  (in violet) decreases with time as some of it is transferred to TTG (in orange).

Every *solid-basalt* tracer has an available mass  $m_{\text{ava}}$  for TTG production at a given time  $t$ :

$$m_{\text{ava},i}(t) = m_{\text{enr},i}(t) (1 - X_{\text{depletion}}). \quad (20)$$

In order to uniformly source the mass of TTG from all the *solid-basalt* tracers present in the cell, a fraction  $\chi$  of this available mass is taken as:

$$\Delta m_{\text{TTG},i} = \chi m_{\text{ava},i} = \chi m_{\text{enr},i} (1 - X_{\text{depletion}}). \quad (21)$$

Combining Eq. 17 and 21 yields

$$\chi = \frac{\Delta M_{\text{TTG}}}{\sum_{i=1}^n m_{\text{enr},i} (1 - X_{\text{depletion}})}. \quad (22)$$

The mass of depleted basalt  $m_{\text{dep}}$  on each *solid-basalt* tracer changes with time as:

$$m_{\text{dep},i}(t + \Delta t) = m_{\text{dep},i}(t) + \Delta m_{\text{dep},i} = m_{\text{dep},i}(t) + \Delta m_{\text{TTG},i} \left( \frac{X_{\text{depletion}}}{1 - X_{\text{depletion}}} \right), \quad (23)$$

and the dimensionless *depletion* value ( $< 1$ ) on each *solid-basalt* tracer is updated as:

$$\text{depletion}_i(t + \Delta t) = \frac{m_{\text{dep},i}(t + \Delta t)}{m_{\text{dep},i}(t + \Delta t) + m_{\text{enr},i}(t + \Delta t)}. \quad (24)$$

This *depletion* gives the amount of depleted and *enriched basalt* in a cell. In the present study, we considered depletion fractions of 0.9 and 0.5, corresponding to basalt-to-TTG production efficiency of 10% and 50%.

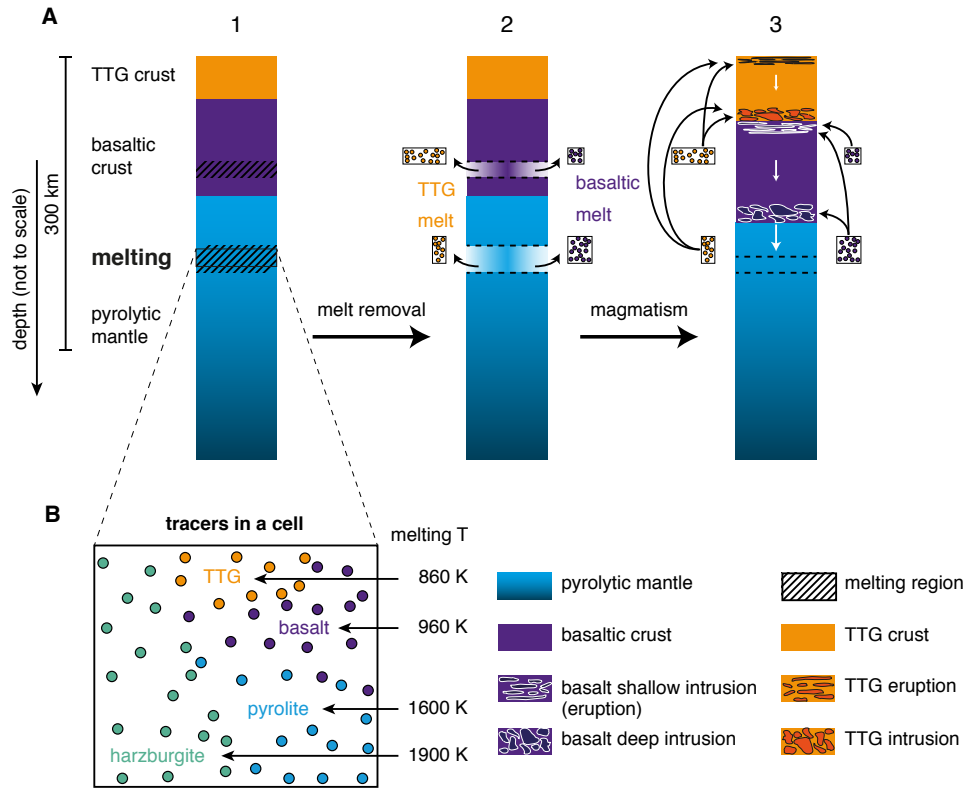


Figure 4: Cartoon depicting a section of a mesh column (not to scale). **A1**, Initial state with TTG crust, basaltic crust, pyrolytic mantle, and the region undergoing melting. **A2**, After melt removal but before compaction or opening gaps in lithosphere for magmatism. **A3**, Final state with the eruption and intrusion of the melt with the white downgoing arrows representing compaction of tracers. **B**, Different melting temperatures (approximations) for different compositions. The aspect ratio (the proportional relationship between its width and its height) of the cells in the model first decreases with increasing depth and then increases again at the core-mantle boundary. Therefore, the cell visualised here is not representative of the entire mesh. Moreover, the number of tracers in a cell vary especially during magmatism.

### 2.4.3. Melt extraction

Fig. 4 illustrates our melt extraction treatment. As we are interested in long-term planetary evolution, the crust production process is simplified as introduced for basaltic crust in Xie and Tackley (2004a) and subsequently used in Nakagawa et al. (2010); Lourenço et al. (2016). At each time step, instantaneous radial transport of melt is assumed and calculated separately in each vertical column of the mesh.

If melt is generated above 300 km depth, it is instantaneously removed for emplacement (Christensen and Hofmann, 1994; Xie and Tackley, 2004a). As described in the previous sections, molten tracers of various compositions appear in each cell (Fig. 4B). The thicknesses of both pre-existing TTG and basaltic crusts are then computed (Fig. 4A1). Molten tracers that have to be transported are removed from the cells and their masses are computed (Fig. 4A2). Non-transport tracers in the entire column are then compacted downwards (represented as downgoing white arrows in Fig. 4A3) to account for the mass loss by removal of molten tracers. Gaps

are created at both the bottom and top of existing TTG and basaltic crusts. The melt is transported both to the bottom of the crust (*plutonism* or *intrusion*) and to the top of the domain (*volcanism* or *eruption*), unless there is already some melt present at the surface (Fig. 4A3). The intruded melt stays molten while a temperature adjustment to account for adiabatic decompression is applied, and tends to result in a warm, weak lithosphere. The erupted melt is rapidly solidified by setting its temperature to the surface temperature (300 K), resulting in a strong and cold lithosphere (Rozel et al., 2017). The mass ratio of erupted to intruded melt can be controlled by the eruption efficiency. Eruption efficiency defines the percentage of mantle-derived melts (or basaltic-crust derived melts in the case of TTG formation) that is erupted at the surface. In nature, the majority of mantle-derived melts intrude at a depth, corresponding to an eruption efficiency between 9% and 20% (Crisp, 1984). It is one of the important parameters being tested in this study. Geological evidence suggests that komatiites have erupted above Archean continental crust in the past (Nisbet, 1982) and basalt frequently erupts above TTG in nature (François et al., 2014). However, the low resolution in our global models would not allow us to resolve such geological features, and therefore our melt extraction treatment does not allow for basalt to erupt above TTG. This could be improved in the future versions of the code.

### 2.5. Volume and Crustal Recycling Rate

At any given time  $t$ , the volume of total TTG produced  $V_{\text{TTG,total}}$  and TTG crust remaining at the surface  $V_{\text{TTG,crustal}}$  are given by:

$$V_{\text{TTG,total}}(t) = \frac{n_y}{\pi} \left( \frac{M_{\text{TTG}}(t)}{\rho_{\text{s,TTG}}} \right), \quad (25)$$

$$V_{\text{TTG,crustal}}(t) = 4\pi d_{\text{TTG}}(t) \left( r_{\text{Earth}} - \frac{d_{\text{TTG}}(t)}{2} \right)^2, \quad (26)$$

with number of cells in lateral direction  $n_y$ , mass of TTG produced  $M_{\text{TTG}}$  and mean global TTG crustal thickness  $d_{\text{TTG}}$  at that time, and radius of Earth  $r_{\text{Earth}}$ . The volume of basaltic crust that remains at the surface or underlies the TTG crust is given by:

$$V_{\text{bas,crustal}}(t) = 4\pi d_{\text{bas}}(t) \left( r_{\text{Earth}} - \frac{d_{\text{bas}}(t)}{2} \right)^2, \quad (27)$$

with mean global basaltic crustal thickness  $d_{\text{bas}}$  at that time. All global volumes reported here are scaled up to represent 3D Earth from 2D simulations to make the comparison with natural data easier. The difference between total and crustal volumes gives the amount of TTG that has been recycled back into the mantle. The rate of recycling of continental crust at time  $t_i$  with timestep  $i = 1, 2, 3..$  is given by:

$$\text{recycling}(t_i) = \frac{(V_{\text{TTG,total}} - V_{\text{TTG,crustal}})_{t_{i+1}} - (V_{\text{TTG,total}} - V_{\text{TTG,crustal}})_{t_{i-1}}}{t_{i+1} - t_{i-1}} \quad (28)$$

As not all simulations reached 4.5 billion years of evolution, final global volumes are not directly comparable. Therefore, global volumes for all simulations after 1 billion years of runtime are given in Table 3 and 4. For volumes generated by all simulations at their final runtime  $t_r$ , see Table D.5 and D.6 in Appendix.

Table 3: First set of simulations with coesite-stishovite phase transition, initial core temperature  $T_{\text{cmb}} = 6000$  K, friction coefficient  $\mu = 0.2$ , depletion fraction  $X_{\text{depletion}}$ , eruption efficiency  $e$  (%), final model runtime  $t_r$  (Gyr), volume of TTG crust  $V_{\text{TTG,crustal}}$ , volume of basaltic crust  $V_{\text{bas,crustal}}$ , and volume of total TTG produced  $V_{\text{TTG,total}}$ . Unless specified, all volumes reported here are in  $\text{km}^3$  after 1 billion years of evolution.

$X_{\text{depletion}}$	$e$	$t_r$	$V_{\text{TTG,crustal}}$	$V_{\text{bas,crustal}}$	$V_{\text{TTG,total}}$
0.5	10	4.34	$4.37 \cdot 10^{10}$	$9.98 \cdot 10^9$	$9.89 \cdot 10^{10}$
0.5 <sup>a</sup>	20	0.85	$2.05 \cdot 10^{10}$	$7.46 \cdot 10^9$	$9.66 \cdot 10^{10}$
0.5	30	3.13	$1.79 \cdot 10^{10}$	$8.55 \cdot 10^9$	$9.03 \cdot 10^{10}$
0.5 <sup>a</sup>	40	0.38	$3.27 \cdot 10^9$	$5.29 \cdot 10^9$	$4.30 \cdot 10^{10}$
0.5	60	4.50	$1.05 \cdot 10^{10}$	$7.08 \cdot 10^9$	$9.09 \cdot 10^{10}$
0.5	80	1.01	$1.04 \cdot 10^{10}$	$7.45 \cdot 10^9$	$8.62 \cdot 10^{10}$
0.5	100	4.50	$9.70 \cdot 10^9$	$6.14 \cdot 10^9$	$8.01 \cdot 10^{10}$
0.9	10	1.58	$4.20 \cdot 10^9$	$6.86 \cdot 10^9$	$2.25 \cdot 10^{10}$
0.9	20	3.15	$2.31 \cdot 10^9$	$7.33 \cdot 10^9$	$2.26 \cdot 10^{10}$
0.9 <sup>a</sup>	30	0.23	$1.45 \cdot 10^9$	$5.81 \cdot 10^9$	$9.50 \cdot 10^9$
0.9 <sup>b</sup>	40	4.41	$2.47 \cdot 10^9$	$4.70 \cdot 10^9$	$2.23 \cdot 10^{10}$
0.9 <sup>a</sup>	60	0.34	$1.08 \cdot 10^9$	$4.56 \cdot 10^9$	$1.69 \cdot 10^{10}$
0.9	80	3.23	$1.59 \cdot 10^9$	$5.32 \cdot 10^9$	$2.23 \cdot 10^{10}$
0.9	100	1.25	$1.73 \cdot 10^9$	$4.67 \cdot 10^9$	$2.14 \cdot 10^{10}$

<sup>a</sup> volumes reported after final model runtime  $t_r$

<sup>b</sup> simulation *e40x9* presented in Fig. 6 and 7

### 3. Results

Two sets of simulations with different depletion fraction values, basalt solidus temperature and phase transitions were performed. All simulations considered compressible convection with core cooling, time-dependent internal heating, melting and crustal production, reference viscosity  $\eta_0 = 10^{21}$  Pa·s and initial mantle potential temperature  $T_{\text{P0}} = 1900$  K. The initial mantle temperature follows an adiabatic profile with thermal boundary layers at top and bottom and has random perturbations (100 K). The heat production from radioactive elements  $H$  in material of primitive composition is initially  $18.77 \cdot 10^{-22}$  W/kg and decreases with time with a half-life of 2.43 billion years. Radioactive material is enriched in the crust during melting (see Section 2.4 for details). First, we ran 14 simulations (Table 3) with depletion fraction  $X_{\text{depletion}} = 0.9$  and 0.5 and coesite-stishovite phase transition (as introduced in Section 2.3). Second, we ran another 21 simulations (Table 4) without coesite-stishovite phase transition and employing a depletion fraction of 0.5 with a slightly different basalt solidus temperature (due to a mistake in a previous publication (Sizova et al., 2015), see Appendix B for details). Overall, we systematically varied the following parameters:

- Depletion fraction  $X_{\text{depletion}}$ : 0.5 and 0.9
- Eruption efficiency  $e$ : 10, 20, 30, 40, 60, 80 and 100%
- Initial core temperature  $T_{\text{cmb}}$ : 5000 and 6000 K
- Friction coefficient  $\mu$ : 0.2 and 0.4

Table 4: Second set of simulations with slightly different solidus temperature and depletion fraction  $X_{\text{depletion}} = 0.5$ , initial core temperature  $T_{\text{cmb}}$  (K), friction coefficient  $\mu$ , eruption efficiency  $e$  (%), final model runtime  $t_r$  (Gyr), volume of TTG crust  $V_{\text{TTG,crustal}}$ , volume of basaltic crust  $V_{\text{bas,crustal}}$ , and volume of total TTG produced  $V_{\text{TTG,total}}$ . Unless specified, all volumes reported here are in  $\text{km}^3$  after 1 billion years of evolution.

$T_{\text{cmb}}$	$\mu$	$e$	$t_r$	$V_{\text{TTG,crustal}}$	$V_{\text{bas,crustal}}$	$V_{\text{TTG,total}}$
5000	0.2	10	1.82	$2.75 \cdot 10^{10}$	$8.59 \cdot 10^9$	$7.74 \cdot 10^{10}$
5000 <sup>a</sup>	0.2	20	0.88	$1.23 \cdot 10^{10}$	$5.94 \cdot 10^9$	$6.37 \cdot 10^{10}$
5000	0.2	30	3.81	$1.36 \cdot 10^{10}$	$7.99 \cdot 10^9$	$6.80 \cdot 10^{10}$
5000	0.2	40	2.28	$1.09 \cdot 10^{10}$	$7.43 \cdot 10^9$	$6.44 \cdot 10^{10}$
5000 <sup>x</sup>	0.2	60	2.74	$7.15 \cdot 10^9$	$6.39 \cdot 10^9$	$6.12 \cdot 10^{10}$
5000 <sup>a</sup>	0.2	80	0.43	$1.92 \cdot 10^9$	$4.37 \cdot 10^9$	$3.01 \cdot 10^{10}$
5000	0.2	100	4.28	$5.06 \cdot 10^9$	$5.43 \cdot 10^9$	$5.36 \cdot 10^{10}$
6000	0.2	10	2.78	$2.92 \cdot 10^{10}$	$8.13 \cdot 10^9$	$9.42 \cdot 10^{10}$
6000	0.2	20	2.60	$2.53 \cdot 10^{10}$	$8.39 \cdot 10^9$	$9.38 \cdot 10^{10}$
6000 <sup>b</sup>	0.2	30	4.31	$2.16 \cdot 10^{10}$	$8.21 \cdot 10^9$	$9.22 \cdot 10^{10}$
6000	0.2	40	3.11	$1.32 \cdot 10^{10}$	$6.35 \cdot 10^9$	$8.46 \cdot 10^{10}$
6000	0.2	60	2.70	$1.00 \cdot 10^{10}$	$6.62 \cdot 10^9$	$7.96 \cdot 10^{10}$
6000	0.2	80	4.50	$8.45 \cdot 10^9$	$6.62 \cdot 10^9$	$7.62 \cdot 10^{10}$
6000	0.2	100	4.50	$9.48 \cdot 10^9$	$6.16 \cdot 10^9$	$7.08 \cdot 10^{10}$
6000	0.4	10	2.50	$3.69 \cdot 10^{10}$	$9.86 \cdot 10^9$	$9.74 \cdot 10^{10}$
6000 <sup>x</sup>	0.4	20	1.70	$3.79 \cdot 10^{10}$	$1.10 \cdot 10^{10}$	$9.32 \cdot 10^{10}$
6000	0.4	30	1.29	$2.09 \cdot 10^{10}$	$8.56 \cdot 10^9$	$8.69 \cdot 10^{10}$
6000	0.4	40	2.47	$1.46 \cdot 10^{10}$	$7.62 \cdot 10^9$	$8.34 \cdot 10^{10}$
6000	0.4	60	1.58	$1.01 \cdot 10^{10}$	$7.06 \cdot 10^9$	$7.92 \cdot 10^{10}$
6000	0.4	80	4.39	$7.90 \cdot 10^9$	$6.18 \cdot 10^9$	$7.51 \cdot 10^{10}$
6000	0.4	100	4.50	$9.64 \cdot 10^9$	$6.19 \cdot 10^9$	$7.20 \cdot 10^{10}$

<sup>a</sup> volumes reported after final model runtime  $t_r$

<sup>b</sup> simulation *e30x5* presented in Fig. 8, 9 and 10

<sup>x</sup> excluded from empirical fits owing to data corruption

### 3.1. Crustal growth

Fig. 5 depicts the volume and composition of crusts formed in the subset of simulations that are presented in Table 3 and 4.

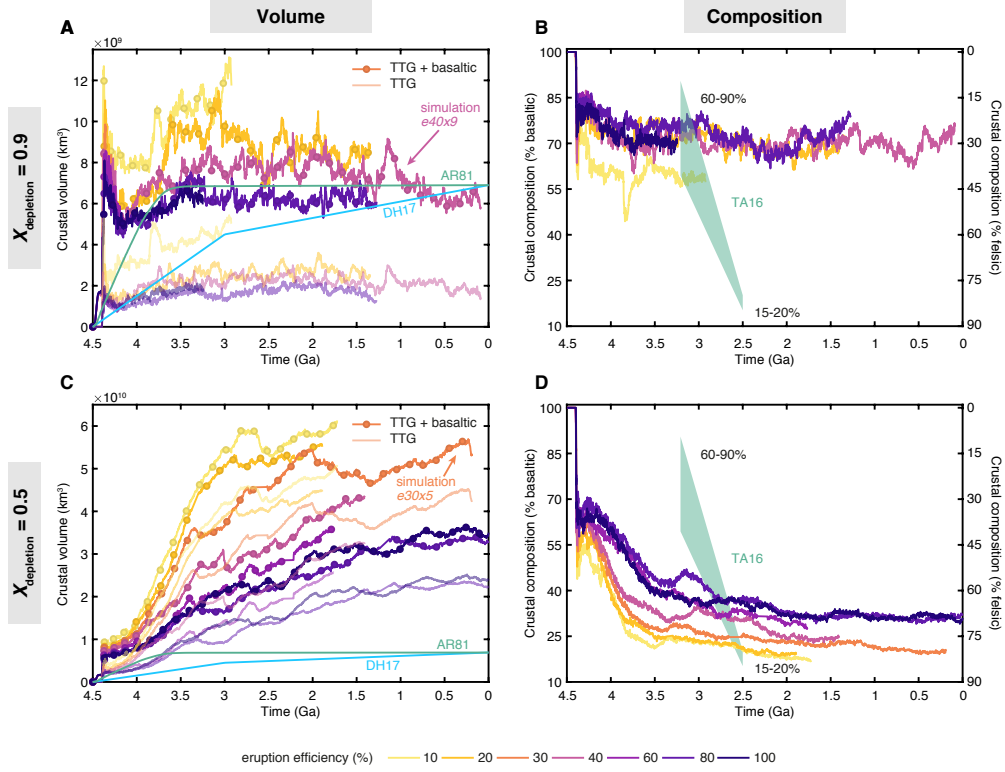


Figure 5: **A, C:** crustal volume of TTG (with different scales on y-axes) for a subset of simulations with  $T_{\text{cmb}} = 6000$  K and  $\mu = 0.2$  presented in Table 3 and 4 respectively. *e40x9* and *e30x5* are the simulations presented in Section 3.2. **B, D:** evolution of composition for the same simulations. Models taken from literature are for net crustal growth (AR81: Armstrong (1981); DH17: Dhuime et al. (2017);) and crustal composition (TA16: Tang et al. (2016)).

#### 3.1.1. Volume of crust

Fig. 5A and 5C show that our simulations using a depletion fraction of 0.9 are able to reproduce the present day volume of continental crust (TTG + basaltic in opaque curves) whereas simulations employing a depletion fraction of 0.5 overestimate crustal production by a factor of 3 to 8, depending on the eruption efficiency (opaque curves). We have compared our modelling results with two different net crustal growth models by Armstrong (1981) (AR81: teal curve) and Dhuime et al. (2017) (DH17: light blue curve), which also take crustal recycling into account. Consistent with previous studies (Crisp, 1984; Cawood et al., 2013; Rozel et al., 2017), we confirm that the volume of felsic crust produced (translucent curves) increases when magmatism is more intrusive.

In all these simulations, the present-day volume of continental crust is generated with the arrival of the first plumes after  $\sim 100$  million years of evolution time. The crustal volume in simulations with large depletion fraction then decreases by 20-40% and later stabilises close to the present-day value after  $\sim 1$  billion years (3.5 Ga) of evolution. Around the same time, a reduction in crustal growth is observed for simulations with low depletion fraction, however, the overall crustal volume continues to increase.

As discussed further in Section 3.3 and 4.1, it is worth mentioning that these modelling results are dependent on the choice of initial conditions, which might also be unrealistic in certain simulations. However, we would like to highlight that changes in crustal growth can happen in our models without a change in the convection regime, and this result holds true for all simulations irrespective of the choice of model parameters.

### 3.1.2. Composition of crust

Fig. 5B and 5D show the evolution of average crustal composition with time. Using MgO content as a proxy for silicification of the Archean crust, Tang et al. (2016) suggested a gradual shift in its average composition from mafic to felsic from early Archean to late Archean (regions shaded in teal), which may predominantly characterise the eroded continental crust emerged above the sea level (Flament et al., 2013). The corresponding basaltic content might have dropped from 60-90% to 15-20%. Tang et al. (2016) hypothesised that a possible onset of plate tectonics around 3.0 Ga would have provided a supply of water to the mafic source material to generate voluminous TTGs and other felsic magmas. Our simulations employing a large depletion fraction are only able to decrease the basaltic content to 60-70%. The simulations with overestimated crustal production are able to follow the proposed trend, however, the shift in composition happens 1 billion years earlier ( $\sim 4.0$  Ga) than the proposed time. While Tang et al. (2016) argue for the operation of plate tectonics around 3.0 Ga as the reason behind the change in crustal composition, we show similar trends in our models without any present-day slab-driven subduction or plate tectonics.

### 3.2. Model evolution

As all simulations presented in Table 3 and 4 show similar behaviour in terms of decompression melting by mantle plumes and the production and recycling of crust, in this section we illustrate the thermal and compositional evolution with time for two representative simulations with  $e = 40$  and 30%,  $X_{\text{depletion}} = 0.9$  and 0.5,  $T_{\text{cmb}} = 6000$  K, and  $\mu = 0.2$  (hereafter, referred to as  $e40x9$  and  $e30x5$  respectively) depicted in Fig. 6, 7, 8, 9 and 10. In both simulations, the generation of TTG can be divided into two distinct stages: a fast growth with intense recycling from 4.5-3.5 Ga followed by a slower growth with moderate recycling. In all these figures, the cell-based composition field represents the following different material: *TTG* ( $\geq 60\%$  in tangerine), *basalt* ( $\geq 60\%$  in dark purple), *harzburgite* ( $\geq 40\%$  in teal, lighter shades represent higher harzburgite content and mantle depletion), *TTG-melt* ( $\geq 50\%$  in peach-orange), *basaltic-melt* ( $\geq 50\%$  in sky blue), *harzburgitic-melt* ( $\geq 50\%$  in white), and *TTG-basalt-mix* ( $\geq 40\%$  *TTG* and  $\geq 40\%$  *basalt* in light purple). The empty cells in black represent mixes of different materials that do not fit either of the above criteria. The relevant parameters are specified in the top-right corner of all the figures in the section.

### 3.2.1. Simulation *e40x9*, employing a high depletion fraction and coesite-stishovite phase transition

Fig. 6 and 7 show two stages of the evolution for simulation *e40x9*, which is able to reproduce a crustal volume similar to the present day value.

In the early stage of the evolution, Fig. 6 shows that the first plumes arriving at the surface cause decompression melting in the upper mantle. This results in the production of basaltic melt while leaving behind a depleted mantle residue with higher harzburgite content. The basaltic melt is both erupted at the surface to form oceanic crust, and intruded at a depth as molten material. The oceanic crust subsequently melts to generate TTG melt at the tip of deformation fronts driven by the lateral spreading of plumes. 40% of this TTG melt solidifies at the surface to make the new felsic crust, while the rest is intruded at the base of existing felsic crust as molten material. The plumes spread laterally when they reach the base of the lithosphere and bring a lot of very warm material with them. Upon cessation of the lateral spreading of the plumes, this warm material cools very quickly by diffusion and crustal production. Most of the basaltic crust and some TTG crust are produced by this process (see the top right side of the bottom panel in Fig. 6). The generation of such a huge amount of crust also depletes the underlying mantle to a large extent. This plume-induced regime leaves the mantle with a bimodal composition: either basaltic or harzburgitic. The newly generated crust and the underlying depleted layer are quickly removed and recycled laterally by the arrival of successive plumes. 100-200 km thick layers of consisting of TTG, basalt and harzburgite are therefore quickly produced and buried. At this stage, large quantities of TTG crust are both generated and recycled back into the mantle. The increase in TTG crust's density by  $168 \text{ kg/m}^3$  at a depth of 290 km also contributes to its recycling. By 4081 Ma, this intense deformation phase has slowed down and TTG crustal volume starts to increase again (as shown in Fig. 5A). The two middle panels of Fig. 6 show that the initial pyrolytic material (darker teal) is brought up and consumed by plumes, whereas layers of basalt, TTG and harzburgite propagate in the whole mantle from the top. Looking at the zoom-in in Fig. 6, large amounts of harzburgitic melt (white) can be seen in the upper mantle. These regions also have molten basalt (sky blue), which is not visualised due to its low concentration (less than 50%).

Fig. 7 illustrates a later stage of planetary evolution in which instances of TTG crust are preserved at the surface (around 1948 Ma) despite the absence of strong cratonic roots in our models. This preservation of TTG can be explained by the absence of pyrolytic material in the lower mantle and a lower core temperature which both decrease the magmatic and mechanical intensity of the plumes. The right panel of the composition plots shows that different compositional layers are being slowly stirred in the mantle, although we employ a rather large reference viscosity in the present study.

### 3.2.2. Simulation *e30x5*, employing a low depletion fraction

As in the previous simulation, the general processes of TTG generation, crustal recycling, delamination and density-driven dripping are apparent. However, there are some noticeable differences in the mantle dynamics and crustal production.

Fig. 8 shows that the initial plumes are not able to spread laterally as much as in the simulations employing a high depletion fraction. This can be explained by the fact that a much larger amount of TTG is being produced, which tends to mechanically limit the lateral spreading of the plumes. Fig. 8 also shows a stage at 3993 Ma in which the intense plume activity has subsided. A number of tentacular structures whose lateral extent can reach up to several hundreds of kms can be seen in the upper and mid-mantle, which are a mix of TTG and basalt-eclogite material

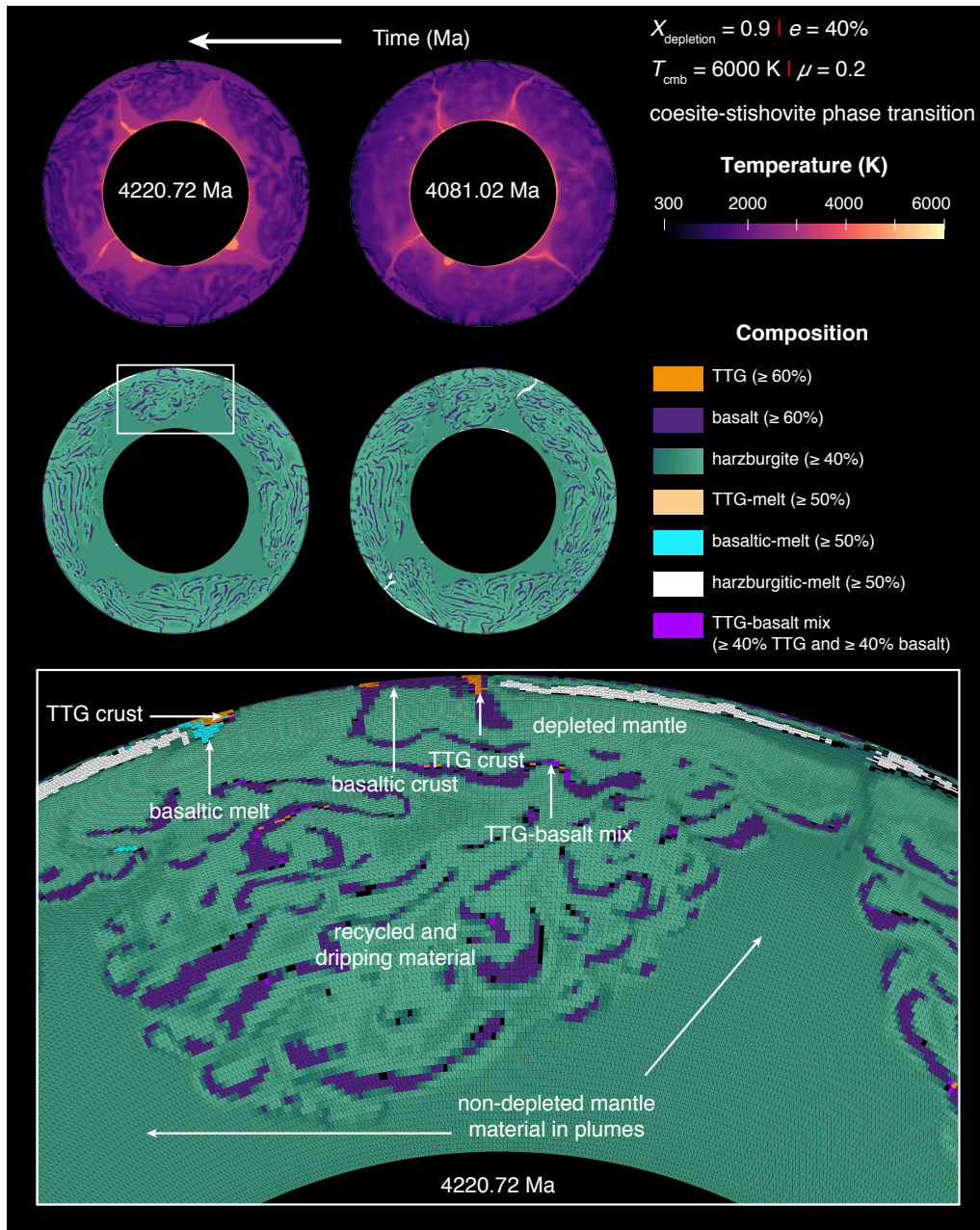


Figure 6: Thermal (*top*) and compositional (*middle* and zoom-in at *bottom*) evolution with time for simulation *e40x9*. The lighter shades of teal in the composition field represent progressive mantle depletion (higher harzburgite content) with time. Continued in Fig. 7.

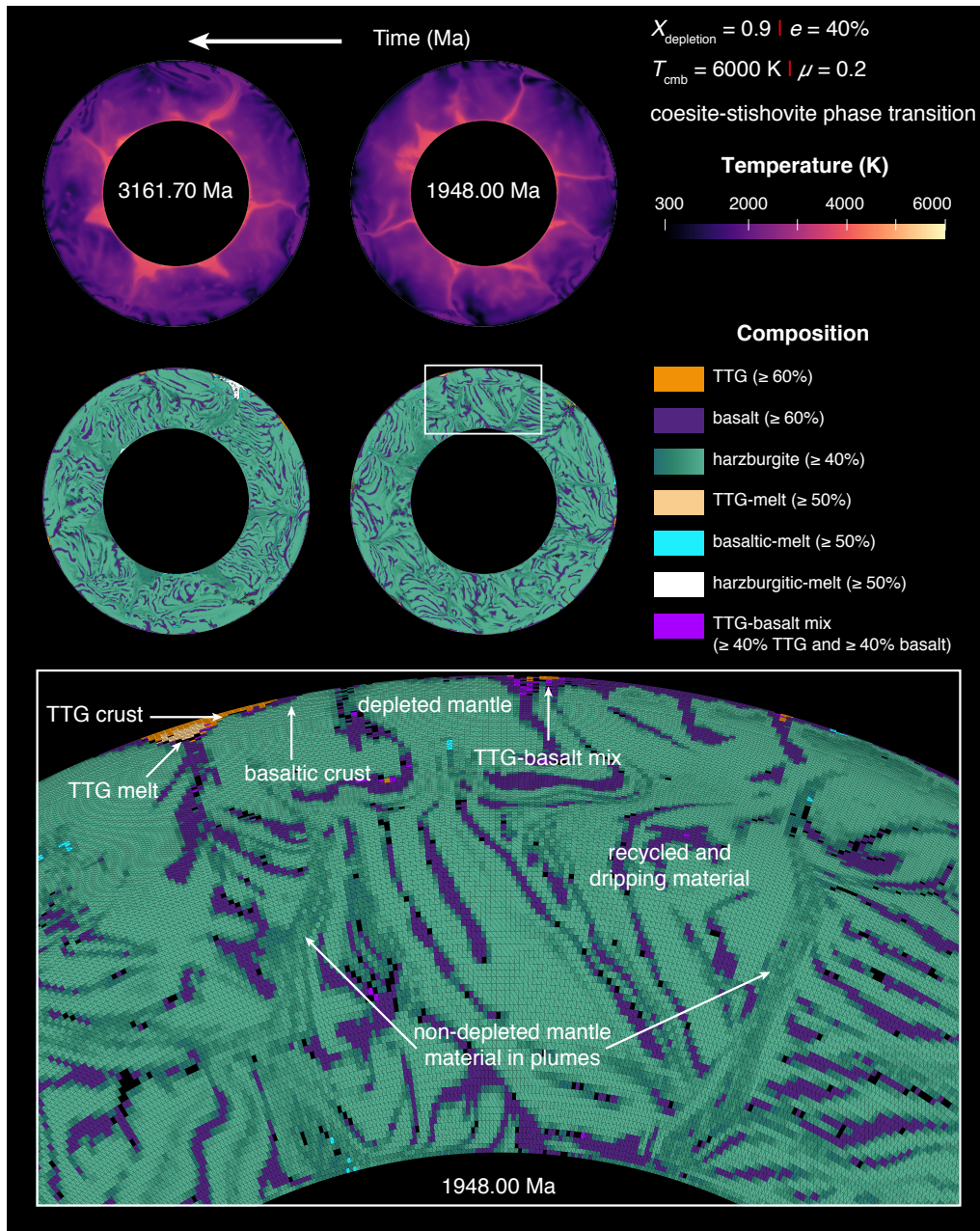


Figure 7: Continued from Fig. 6. Thermal (*top*) and compositional (*middle* and zoom-in at *bottom*) evolution with time for simulation *e40x9*. The lighter shades of teal in the composition field represent progressive mantle depletion (higher harzburgite content) with time.

with different densities. Without the inclusion of the coesite-stishovite phase transition in this simulation, this mix material is neutrally buoyant and does not sink to the bottom of the mantle. Around 3506 Ma (see Fig. 9), TTG crust has covered a large portion of the surface. The core temperature has cooled down to about 5000 K and the plumes have become weaker. By 2995 Ma, TTG crust covers most of the surface and is underlain by basaltic crust. There are chunks of basaltic material dripping down into the mantle and many tentacular structures exist.

Fig. 10 shows the compositional and thermal evolution of the same simulation for a period of 25 million years. Around 3392 Ma, a plume reaches the surface, resulting in a large scale decompression melting event. The pre-existing basaltic and TTG crust are pushed aside and compressed together to form structures that are perhaps similar to stacked terranes found in the Eoarchean Era (Bédard, 2006). It has been suggested that such granite-greenstone terranes formed in the convergent margins and accounted for the stable cratonic interiors of continents (Kusky and Polat, 1999). However, these terranes are produced in our models without the need for present-day subduction and do not impart any stability to the overlying TTG crust. Typical granite-greenstone terranes (TTG+basalts+komatites) observed in nature are of the order of few hundreds of km and hence our models are comparable to them.

### 3.3. Influence of other model parameters

#### 3.3.1. Eruption efficiency

The volumetric percentage of mantle-derived melt erupted as surface volcanism is given by the eruption efficiency. It has previously been shown in numerical simulations that eruption efficiency has an influence on the pressure-temperature conditions of TTG melt formation (Sizova et al., 2015; Fischer and Gerya, 2016). Fig. 11A and 11C show that the total and crustal volumes of TTG in our simulations depend on the eruption efficiency in the first 1 billion years. The cold and thick basaltic crust created as a result of volcanism by high eruption efficiency (Moore and Webb, 2014; Lourenço et al., 2016; Rozel et al., 2017) is not warm enough to coincide with TTG formation conditions. With low eruption efficiency, more melt is intruded at depths, creating a warmer basaltic crust. This crust melts to form TTG in the presence of water and *enriched basalt*. The recycling of crustal material depicted in Fig. 11B and Fig. 11D is discussed in section 4.1.2.

#### 3.3.2. Initial core temperature

Compared to the simulations with an initial core temperature of 6000 K, a value of 5000 K results in lower production of basaltic and TTG material (Fig. 12A). A lower core temperature makes the initial plumes weaker and the recycling rates are slightly lower (Fig. 12B). The crustal growth follows a parabolic curve representing the initial phase of intense convective activity until 3.5 Ga.

#### 3.3.3. Friction coefficient

The internal friction coefficient  $\mu$  of the lithosphere has been shown to influence global and regional lithospheric dynamics (e.g., Tackley, 2000; Gerya et al., 2015). We use a higher value of 0.4 in some of our simulations (see Table 4) and observed negligible differences. The crustal growth followed the same two stages (not shown here) as with a value of 0.2 (discussed in Section 3.2 and shown in Fig. 5) and the total volume of TTG produced is comparable to the volumes given by simulations with a lower friction coefficient. This is because the value of 0.2 is already too high for subduction and mobile plates to be produced; most lithospheric deformation is a result of weakening by plutonic magmatism rather than yielding.

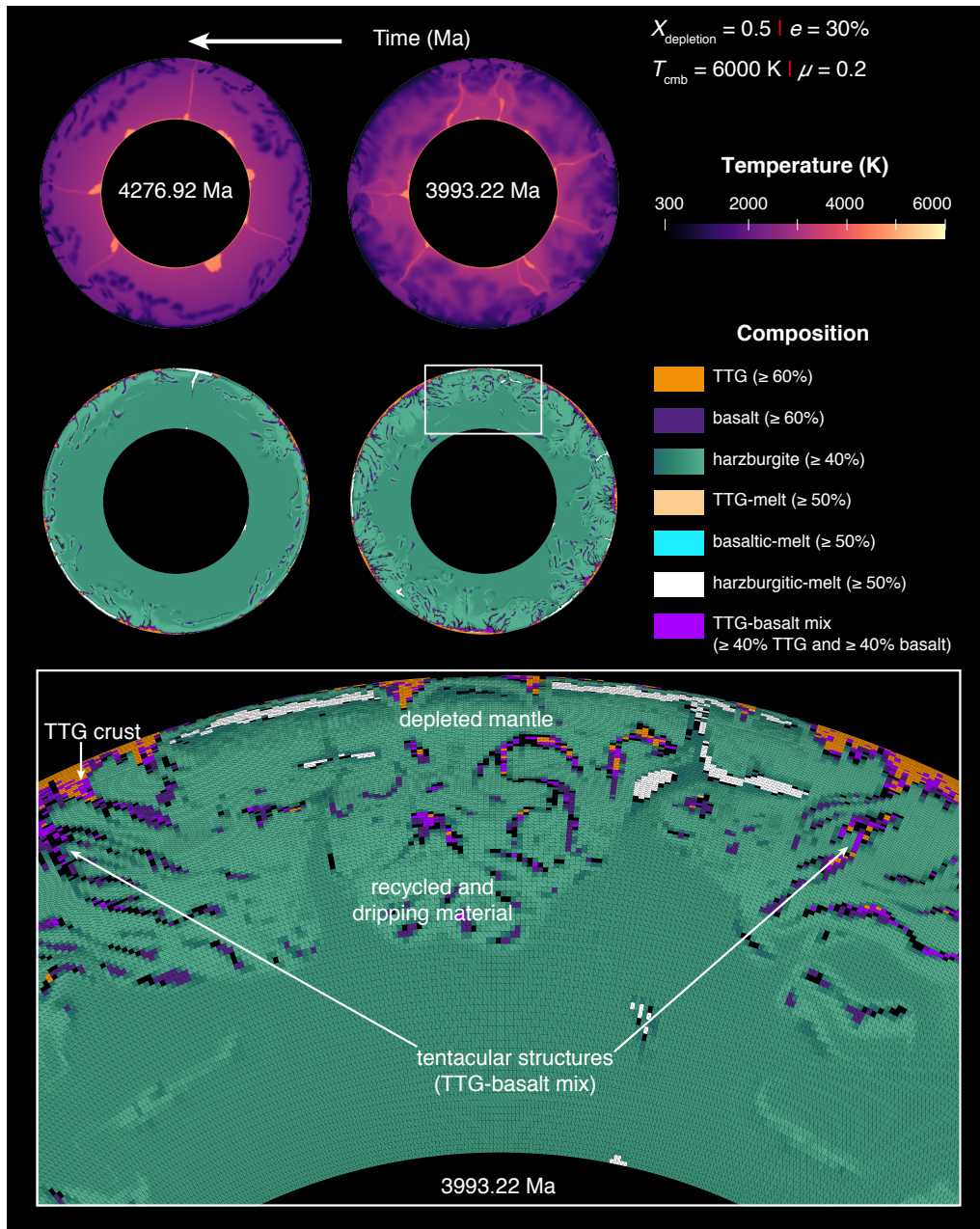


Figure 8: Thermal (*top*) and compositional (*middle* and zoom-in at *bottom*) evolution with time for simulation  $e30x5$ . The lighter shades of teal in the composition field represent progressive mantle depletion (higher harzburgite content) with time. Continued in Fig. 9.

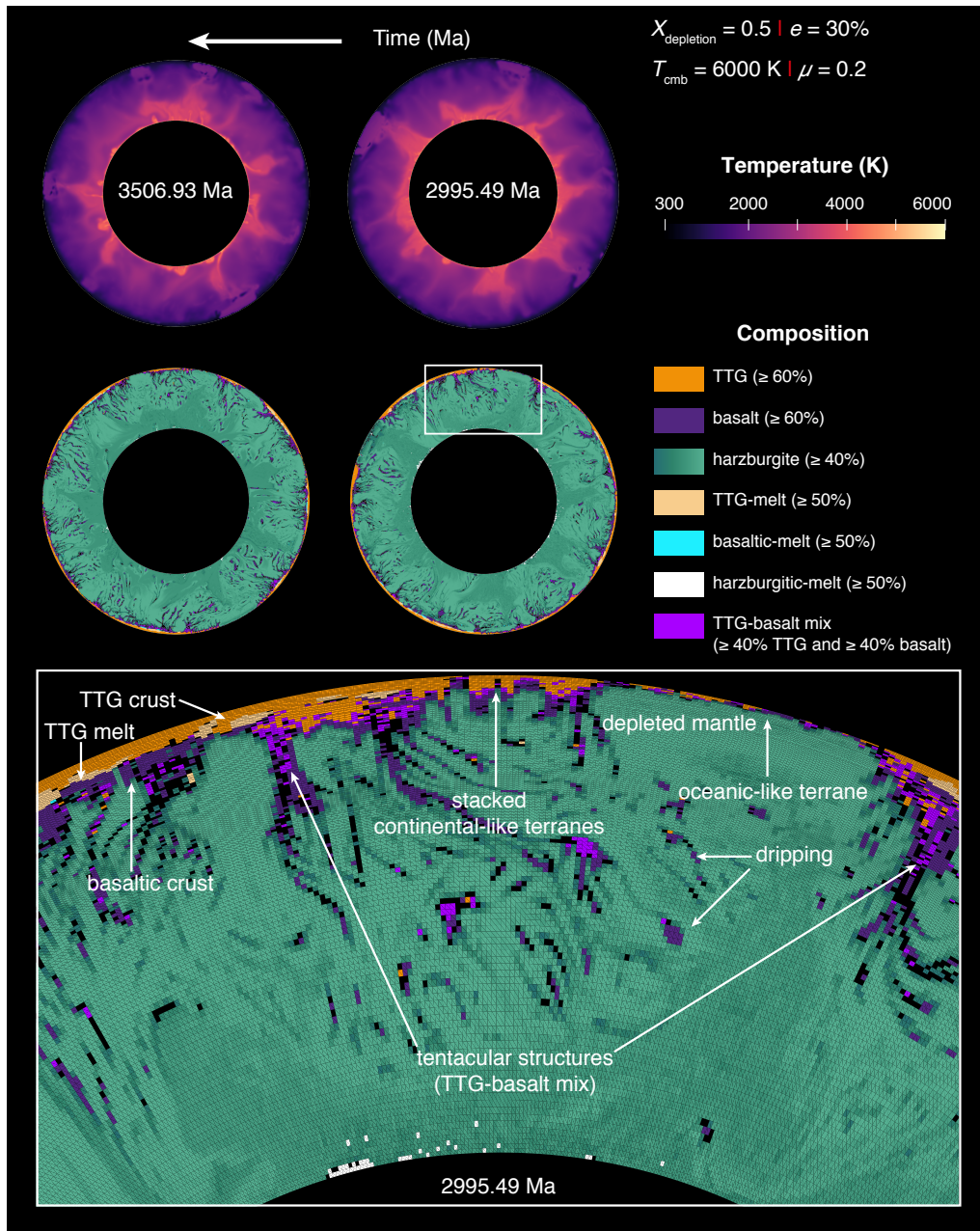


Figure 9: Continued from Fig. 8. Thermal (*top*) and compositional (*middle* and zoom-in at *bottom*) evolution with time for simulation *e30x5*. The lighter shades of teal in the composition field represent progressive mantle depletion (higher harzburgite content) with time.

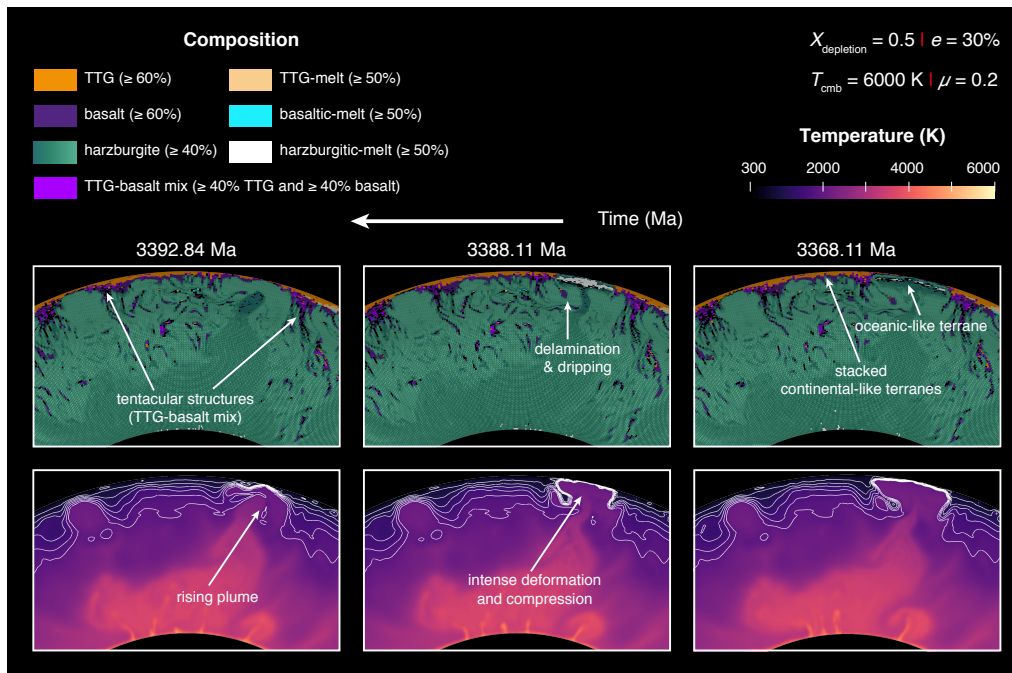


Figure 10: Formation of stacked continental-like terranes over a period of 25 million years for simulation  $e30x5$ . The lighter shades of teal in the composition field represent progressive mantle depletion (higher harzburgite content) with time. White lines are isotherms shown from 900-1900 K with increments of 200 K.

## 4. Discussion

### 4.1. Comparison with continental crust growth models

Despite the fact that plate tectonics does not start in our simulations, and under the assumption that felsic material mostly tends to stay trapped in the lithosphere, comparing the volume of TTG produced in our global numerical simulations with continental crust growth models is a good metric to highlight their significance. However, one must consider that these results may vary with initial conditions or choice of model parameters, as illustrated in Section 3.3. Moreover, care should be taken while making this comparison as some models (e.g., Allègre and Rousseau, 1984; Condie and Aster, 2010) based on geological proxies only provide records of continents preserved today, whereas other models do consider crustal recycling (Roberts and Spencer, 2015; Hawkesworth et al., 2016; Spencer et al., 2017). As the models presented in this study take both crustal production and recycling into account, comparing them with the latter models is more suited. A quick comparison between the continental crust volumes obtained from our simulations and the two net growth models shows that they can both have the same order of magnitude, which is dependent on several model parameters. In this section, we comment on the robustness of these parameters and discuss how they might influence TTG production and/or recycling.

Continental crust growth should take into account the new volume being created by magmatic processes as well as the amount recycled back into the mantle by tectonic erosion and lower crustal delamination (Cawood et al., 2013; Spencer et al., 2017). A range of continental

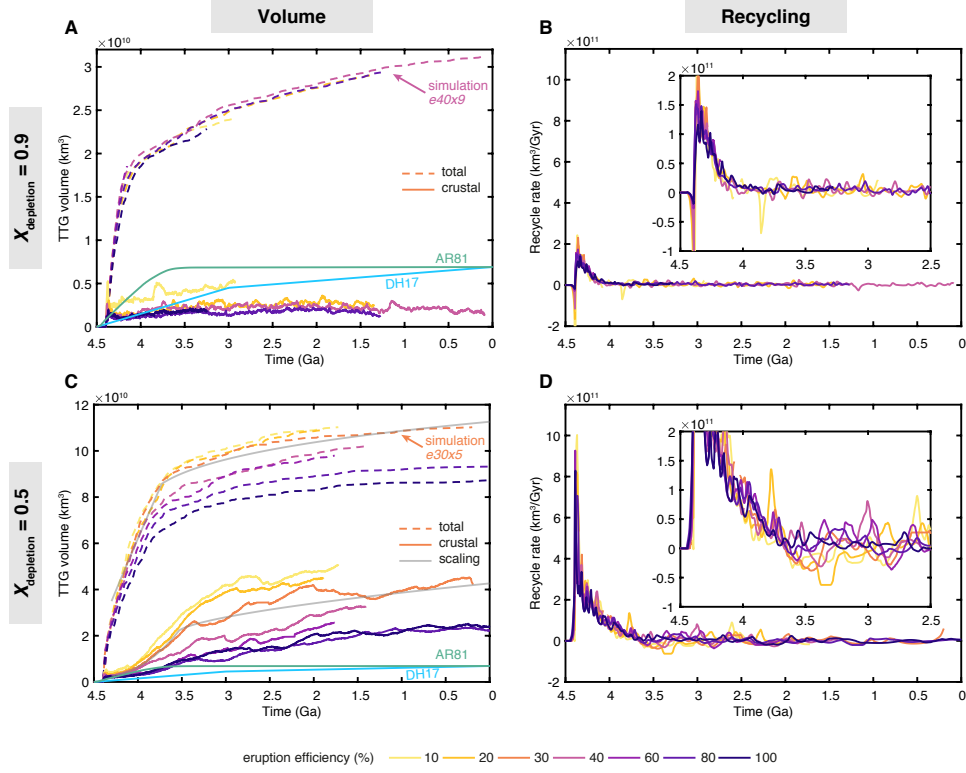


Figure 11: **A, C:** total and crustal volume of TTG (with different scales on y-axes) for a subset of simulations with  $T_{\text{cmb}} = 6000 \text{ K}$  and  $\mu = 0.2$  presented in Table 3 and 4 respectively. Empirical fits of the simulation *e30x5* are shown in grey. **B, D:** crustal recycling rate with insets showing a close up of the oscillations for the same simulations.

crust growth models have been developed on the basis of age distribution and isotopic compositions of rocks. These models fall into two competing camps based on the nature of crustal growth: continuous growth with differing growth rates through Earth history (e.g., Hurley and Rand, 1969; Armstrong, 1981; Allègre and Rousseau, 1984; Taylor and McLennan, 1985; Armstrong, 1991; Taylor and McLennan, 1996; Belousova et al., 2010; Dhuime et al., 2012); versus episodic growth corresponding to supercontinent cycles or mantle plume activity (e.g., McCulloch and Bennett, 1994; Condie, 1998, 2000, 2004; Rino et al., 2004; Campbell and Allen, 2008; Voice et al., 2011). Using growth models built on records of detrital zircons and sedimentary rocks, which may predominantly characterise the eroded continental crust emerged above the sea level (Flament et al., 2013), Dhuime et al. (2017) proposed that 65% of the present continental crust existed by 3 Ga. They argued that there has been a continuous growth of continental crust throughout the evolution of the planet with a significant drop in net production rate from  $2.9 - 3.4 \text{ km}^3 \text{ yr}^{-1}$  on average to  $0.6 - 0.7 \text{ km}^3 \text{ yr}^{-1}$  on average at around  $\sim 3 \text{ Ga}$ .

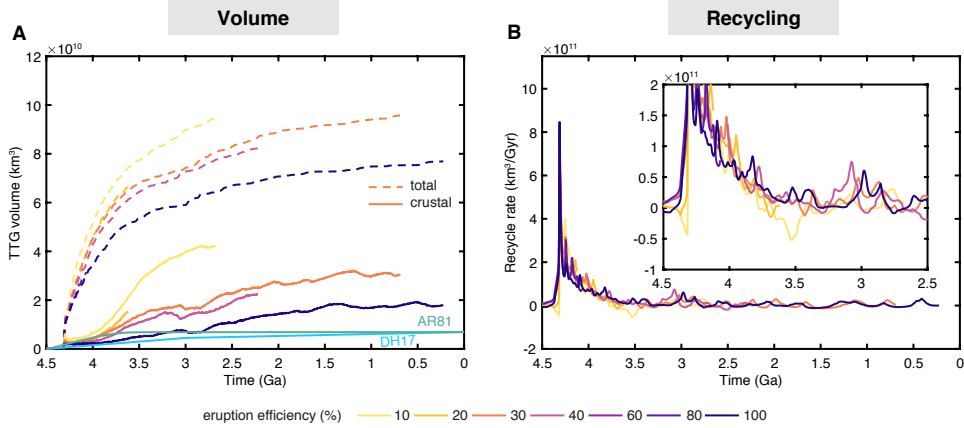


Figure 12: **A:** total and crustal volume of TTG for simulations with  $X_{\text{depletion}} = 0.5$ ,  $T_{\text{cmb}} = 5000 \text{ K}$ ,  $\mu = 0.2$  presented in Table 4. **B:** crustal recycling rate with insets showing a close up of the oscillations for the same simulations.

#### 4.1.1. Crustal volume and composition

Firstly, we would like to remind the reader that our results were obtained in a 2D domain. Although the reported crustal volumes can be compared to the natural data as they have been projected in 3D (see Eqs. 26 and 27), one should keep in mind that the geodynamical regime obtained in a 3D domain might be different from what we observed in a 2D simulation. In particular, while subduction zones and rifts are well represented in 2D, the impact of plumes on the convection and lithosphere dynamics tends to be over-estimated. In the Earth, when a plume reaches the lithosphere, it can spread in a horizontal plane. In our models, plume heads only dissipate in one dimension (i.e., either left or right when reaching the surface), which makes them warmer and more buoyant than what they would be in 3D. This is an important limitation of our models as most of the TTG crust is produced on the edges of these laterally spreading plumes. The amount of TTG produced in the models presented here is therefore probably too large. This could explain why our simulations employing a depletion fraction of 0.5 generate a lot more TTG than what is suggested by the geological record (see Fig. 5C, D).

In all simulations presented here, TTG crustal growth (Fig. 5A and 5C) clearly shows two stages of formation (more details in Appendix E.2). The first is a quasi-parabolic growth, which lasts until around 3.8-3.5 Ga. Afterwards, the growth curve follows a quasi square root of time. This two-stage growth is akin to the proposal of Dhuime et al. (2017). However, the drop in TTG production occurs about 500 million years earlier in our simulations and interestingly, occurs without the initiation of present-day slab-driven subduction or plate tectonics.

Dhuime et al. (2017) considered two different types of continental crust in their crustal growth calculations: mafic, thin, dense crust formed before 3 Ga, and thick, buoyant crust with intermediate composition formed after 3 Ga. In our simulations, we do not model the progressive evolution of the crust's composition from mafic to intermediate over time. Yet, we can distinguish between basaltic (mafic, oceanic) crust and TTG (felsic, continental) crust as they are being generated, and estimate the change in global average crustal composition with time as shown in Fig. 5B and 5D. The very first plumes generate a crust which is entirely basaltic in nature around 4.4 Ga. Following their arrival, a growth in felsic crust is observed lasting about 1 billion

years. This results in a linear shift in the average global crustal composition from basaltic to felsic. The final basaltic content of the crust changes with the volume of TTG crust, which in turn is a function of the eruption efficiency. Using MgO content as a proxy for silicification of the bulk Archean crust, Tang et al. (2016) suggested a gradual shift in its average composition from mafic to felsic between 3.2-2.5 Ga. The corresponding basaltic content might have dropped from 60-90% to 15-20%. Our simulations employing a high depletion fraction of 0.9 are only able to decrease the basaltic enrichment down to 60-70% (Fig. 5B). The simulations with much higher crustal production are able to reproduce the trend proposed by Tang et al. (2016) (Fig. 5D), although it happens  $\sim 1$  billion years earlier.

According to Dhuime et al. (2017), the volume of continental crust after the first 1.5 billion years (timing of inflection as defined in their paper) of Earth's evolution would be  $\approx 4.5 \cdot 10^9 \text{ km}^3$ , or 65% of the present-day volume estimate  $\approx 6.9 \cdot 10^9 \text{ km}^3$ . After 3.5 Ga (timing of inflection in our simulations), the overall volume of TTG and basaltic crust ( $V_{\text{TTG,crustal}} + V_{\text{bas,crustal}}$  from Table 3) in our simulation *e40x9* is  $7.17 \cdot 10^9 \text{ km}^3$ , which has the same order of magnitude as different crustal growth models (Armstrong, 1981; Dhuime et al., 2017) (Fig. 5A). For simulations with  $X_{\text{depletion}} = 0.9$ , the volumes of both TTG and basaltic crust reach a peak in the first 150 million years before being recycled owing to strong plume activity. Following this, crustal volumes remain roughly at the same level throughout the evolution, which is attributed to the episodic generation and recycling of the crust. On average, for simulations with  $X_{\text{depletion}} = 0.5$ , this overall crustal volume is 5-10 times higher (depending on eruption efficiency) than the estimates of crustal growth models (Fig. 5C).

A factor that directly influences the production of TTG in our simulations is the availability of water in the mantle. For simplicity, the material within the top 10 km of the mantle is considered to be fully hydrated at the time of initialisation, and this water is free to advect on tracers throughout the mantle (see Fig. A.13A in Appendix). In the simulations presented here, the concentration of water is taken to be the same (with partition coefficient  $D_{\text{part,H}_2\text{O}} = 1$ ) in both the solid and melt phases. In nature, water is incompatible in the solid phase and partitions into the melt during partial melting. For future work, lower values of  $D_{\text{part,H}_2\text{O}} : 0.01, 0.1$  should be explored as this will substantially reduce the amount of water available in a cell for TTG production with subsequent partial melting events. Additionally, a water-dependent basalt solidus should be used as the presence of water lowers the melting temperatures. Also, depth and temperature limits for water penetration could be applied, as previously done by Gregg et al. (2009) for hydrothermal fluid circulation in their melt migration study.

Simulations presented in this study can produce TTG with a mass of up to  $\approx 4.04 \cdot 10^{23} \text{ kg}$  (10% of mantle mass for  $X_{\text{depletion}} = 0.5$ ) or  $\approx 8.08 \cdot 10^{22} \text{ kg}$  (2% of mantle mass for  $X_{\text{depletion}} = 0.9$ ). Using a reference density of TTG of  $2700 \text{ kg/m}^3$ , these mass limits would correspond to volume limits of  $1.49 \cdot 10^{11} \text{ km}^3$  and  $2.99 \cdot 10^{10} \text{ km}^3$  respectively. However, this physical limit is not the reason for the drop in TTG production at the inflection point in our simulations as none of them produce this much TTG after 1 billion years of evolution (see  $V_{\text{TTG,total}}$  in Table 3, 4 and Fig. 11A, 11C, 12A). For example, assuming that the volume of total TTG produced  $V_{\text{TTG,total}} \approx 1 \cdot 10^{11} \text{ km}^3$  at the end of a simulation (actual values given in Table D.5, D.6) and using Eq. 25, the mass of TTG produced  $M_{\text{TTG}}$  will be  $\approx 8.28 \cdot 10^{20} \text{ kg}$  in that simulation which is only 0.02% of the mass of Earth's mantle. The production of TTG occurs as a result of the plumes, fed by material with a pyrolytic composition (non-depleted mantle material), at the start of our simulations. Over 1 billion years of evolution, the mantle material becomes depleted (represented as lighter shades of teal in compositional field in Fig. 6, 7, 8, 9 and 10) and thus the basalt available in the upper mantle is not enriched enough to produce large quantities of TTG.

Table F.8, F.9 and Fig. F.16 show the final masses and volumes of each type of TTG produced for the first set of simulations presented in Table 3. Fig. F.16 shows that our simulations always produce large amounts of low pressure TTGs (30 to 300 million km<sup>3</sup>) while significantly less medium and high pressure TTGs are generated. In particular, the amount of high pressure TTGs is about 2 orders of magnitude lower than low pressure TTGs. Eruption efficiency seems to have a very weak impact on the amount of each type of TTG produced, which is in strong disagreement with our previous estimations (Rozel et al., 2017).

The weak production of high pressure TTGs in our simulations can be explained by the fact that basalt which reaches high pressure levels might have already passed through low and medium pressure TTG production windows. This indicates that high pressure TTG formation might be intrinsically linked to processes that are not present in the models presented in this study, such as dome and keel destabilisation and/or formation of stable cratonic lithosphere. The lack of high pressure TTG rocks cannot be related to the absence of water at large depths as dehydration during the melting process has been neglected in these simulations. At this point, further investigations are necessary to shed light on which process will enable the generation of medium and especially high pressure TTGs in numerical models of mantle convection.

#### 4.1.2. *Crustal recycling and tectonic settings*

All our simulations show intense recycling of the TTG and basaltic crust with delamination and eclogitic dripping in the first ~500 million years (Fig. 11B, 11D and 12B). This behaviour is similar to the “plutonic squishy lid” or vertical-tectonics geodynamic regime that has been suggested for the early Earth (e.g., Van Kranendonk et al., 2004; Sizova et al., 2010; Johnson et al., 2013b; Gerya et al., 2015; Condie, 2018; Fischer and Gerya, 2016; Lourenço, 2017). The rate of recycling continues to decrease until 3.5 Ga and becomes roughly constant, with small oscillations. The positive fluctuations in recycling rate are attributed to buoyant TTG material being brought back upwards by the convecting mantle and some of it being relaminated to the base of the crust. Negative fluctuations correspond to the delamination and dripping of the lower crust owing to plume activity.

Whether subduction was necessary (e.g., Foley et al., 2003; Arndt, 2013; Martin et al., 2014; Hastie et al., 2015) or not (e.g., Atherton and Petford, 1993; Smithies, 2000; Bédard, 2006; Bédard et al., 2013; Zhang et al., 2013; Qian and Hermann, 2013; Johnson et al., 2013a, 2017) for the genesis of Archean TTGs remains a matter of debate and is closely interlinked with the uncertainty behind the onset of plate tectonics. Since we observe plume driven tectonics rather than long-lived slab pull in our simulations, we can say that none of our simulations exhibit modern-style plate tectonics and yet they are capable of generating Archean TTGs and show a drop in production rate. Based on these results, we argue that present-day subduction was not required for the genesis of primordial continental crust.

A factor that might increase continental crust recycling in our simulations is the inclusion of additional phase transitions. For example, when TTG/felsic material is buried or subducted, its density increases by about 168 kg/m<sup>3</sup> at a depth of 290 km (coesite-stishovite phase transition given in Akimoto and Syono (1969); Akaogi and Navrotsky (1984); Gerya et al. (2004); Ono et al. (2017)). A treatment of all the relevant phase transitions leads to an even higher density increase, with TTG likely becoming denser than basalt throughout most of the upper mantle, and having a density similar to pyrolite in the lower mantle (Komabayashi et al., 2009; Kawai et al., 2009). When the coesite-stishovite phase transition is incorporated in the simulations given in Table 3, no more tentacular structures are observed in the mantle (Fig. 8, 9 and 10). Using a reference viscosity one order of magnitude lower than the value used in the simulations here

( $10^{21}$  Pa·s as shown in Fig. A.13C in the Appendix) would result in a higher convective vigour, which may also increase the recycling rate by thinning the lithosphere (Rozel et al., 2017).

Figure A.13D in the Appendix shows the age of the mantle based on the time since it last melted. The majority of TTG crust (black contour lines) is less than 200 Ma old. This relatively young age of the continental material is because of the constant moderate recycling and its inability to stay preserved and form strong continents. Most of the continental crust has melted again and solidified over time.

#### *4.2. Model limitations and possible future improvements*

These models represent an important step forward in the quest for achieving self-consistent primordial continental crust production in global Archean geodynamics. However, they have some limitations, which should be addressed in future studies. First, the presence of water, which is a requisite for TTG production, has a rather simplified treatment at present. Possible improvements would be to incorporate a reduction in density, viscosity, and melting temperature of rocks based on the water concentration. Second, migrating these models to a three-dimensional domain would limit the impact of plumes on lithosphere dynamics, and possibly result in a lower TTG crust production. Third, forming a stiff subcontinental lithospheric mantle (SCLM) underlying the TTG crust would help in reducing its recycling and ensuring its preservation. It has been suggested that low density, viscous, and melt depleted SCLM might have co-evolved with the continental crust (Herzberg, 1993; Griffin et al., 2003; Griffin and O'Reilly, 2007; Arndt et al., 2009; Lee et al., 2011). Presently, we do not form such rheologically strong cratonic roots in our models (e.g., Beall et al., 2018), possibly because the rheology is not composition-dependent and therefore the depleted harzburgitic material has the same viscosity as the background mantle. Fourth, our simple petrological model could be adapted to consider magmatic weakening or a density increase of the residue after melt extraction (e.g., Sizova et al., 2010; Vogt et al., 2012; Sizova et al., 2015). And finally, increasing the resolution of our global simulations would allow us to reproduce dome and keel structures, which are typical of some Archean cratons (Van Kranendonk et al., 2004; Hickman, 2004; Van Kranendonk, 2011).

## **5. Conclusions**

We have presented here a new numerical modelling approach allowing for the self-consistent creation of primordial continental crust (TTG) in global mantle convection models, for the first time, to our knowledge. This is achieved by parameterising the processes of melt generation and melt extraction. Two distinct stages of TTG production are observed in our simulations: a period of continuous linear growth with time and intense recycling fuelled by strong plume activity and lasting for  $\sim 1$  billion years, followed by a stage with reduced TTG growth and moderate recycling. A general observation in all our simulations is the lateral spreading of the plumes at the surface, which forces parts of the lithosphere to drip (delaminate) into the mantle. We see TTG production happening at the tip of these deformation fronts. A drop in TTG production occurs as the mantle material becomes depleted over time with successive partial melting events and without needing a significant change in the convection regime. Based on these results, we support the idea of plutonism dominated tectonic regime for early Earth and we argue that present-day slab-driven subduction processes were not necessary for the genesis of Archean TTGs. This has significant implications for comparative planetology and the ongoing debate about the onset of modern style subduction-driven plate tectonics. Our simulations and empirical

regressions support the important role of intrusive magmatism in shaping the Earth’s lithosphere (Crisp, 1984; Cawood et al., 2013; Rozel et al., 2017). Most significantly, crustal (mafic basaltic and felsic TTG) volumes obtained from our simulations with lower basalt-to-TTG production efficiency (10%) have the same order of magnitude as with other published net crustal growth models based on geological proxies (Armstrong, 1981; Dhuime et al., 2017). Our simulations with higher basalt-to-TTG production efficiency (50%) are able to reproduce crustal silicification as proposed by Tang et al. (2016). We show lower crustal delamination and dripping, formation of stacked continental-like terranes, and recycling of the continental crust. Future improvements should allow us to reproduce and explain the coeval formation of strong, depleted, and viscous cratonic roots.

## Appendix A. Additional cell- and tracer-based fields for simulation *e40x9*

### Appendix B. Solidus and liquidus temperatures

We detail here the various solidus and liquidus functions used in the present study. In all the functions, pressure  $P$  is in GPa, depth  $d$  is in km, and  $T$  is in K.

#### Appendix B.1. Basalt melting

##### Appendix B.1.1. Below 5 GPa

For pressures up to 5 GPa, the pressure-dependent solidus and liquidus functions for “hydrated basalt” (as defined in their paper) composition are taken from Table 1 of Sizova et al. (2015):

$$T_{\text{sol,bas}}(P)[K] = \begin{cases} 973 - \frac{70,400}{1000P+354} + \frac{77,800,000}{(1000P+354)^2}, & \text{for } P < 1.6 \\ 935 + 3.5P + 6.2P^2, & \text{for } 1.6 \leq P < 5 \end{cases}, \quad (\text{B.1})$$

$$T_{\text{liq,bas}}(P)[K] = 1423 + 105P. \quad (\text{B.2})$$

While analysing the results, we realised that we used a basalt solidus that was shifted towards higher temperatures by 100-200 K (for pressures up to 1.6 GPa). This happened due to a publication error of Eq. B.1 in Sizova et al. (2015) and such a shift in the solidus temperature can be considered as having a lower water content in the mantle (or dry basalt solidus), which remains a big unknown. We made the necessary corrections in order to lower the solidus temperature and ran additional simulations (presented in Table 3), whose results showed that this small error had a minimal impact on the overall TTG produced and its crustal growth (compare panels in Fig. B.14).

##### Appendix B.1.2. Above 5 GPa

For pressures between 5-135 GPa (up to core-mantle boundary), the pressure-dependent solidus and liquidus functions for “mid-oceanic ridge basalt” (as defined in their paper) composition are taken from Fig. 2 of Andraut et al. (2014):

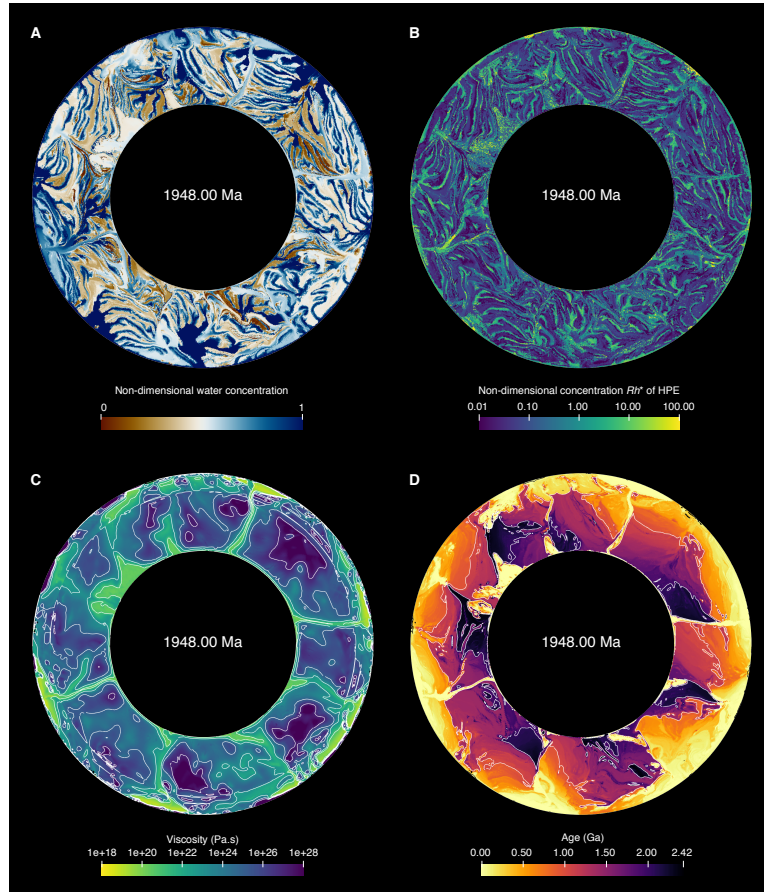


Figure A.13: For simulation *e40x9*, **A**, tracer-based field showing the amount of water in the mantle. The non-dimensional concentration is relative with 1 implying fully hydrated and 0 meaning no water. **B**, tracer-based field showing the non-dimensional concentration of heat-producing element  $Rh^*$  with higher values (yellow) in the crust at the surface. The dimensional concentration  $Rh$  can be computed as  $Rh = Rh^* H e^{-\lambda t}$  with initial internal heating rate  $H$ , time  $t$  and decay constant  $\lambda = 1/t_{\text{half}}$ . **C**, cell-based viscosity field with white contours showing regions with the same viscosity from  $10^{20}$ - $10^{26}$  Pa.s with multiples of 100. **D**, cell-based field showing the age of the mantle based on the time since it melted last. The white contours show parts of the mantle with the same age (1 Ga and 2 Ga). The black contours highlight TTG crust ( $\geq 60\%$  in a cell) and its relatively young age.

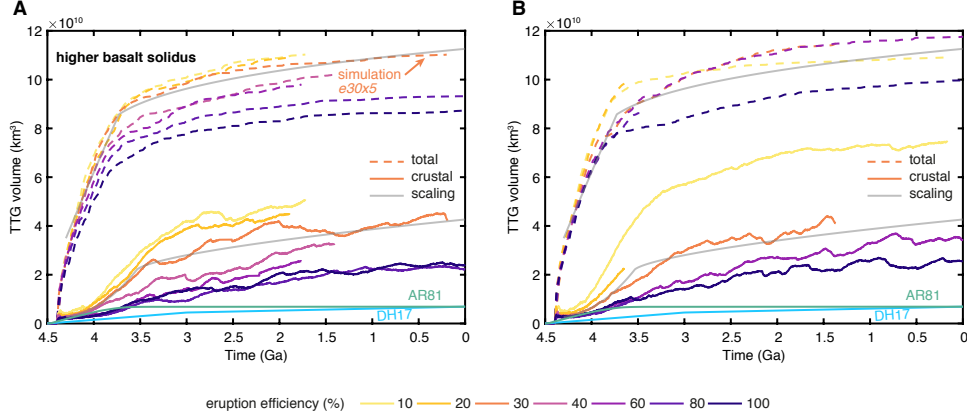


Figure B.14: **A, B**: total and crustal volume of TTG for simulations with different basalt solidus temperature,  $X_{\text{depletion}} = 0.5$ ,  $T_{\text{cmb}} = 6000$  K and  $\mu = 0.2$  presented in Table 4 and 3 respectively. Empirical fits of the simulation *e30x5* are shown in grey.

$$\begin{aligned}
 T_{\text{sol,bas}}(P)[K] &= (-1.0116 \cdot 10^{-12})P^7 + (8.9986 \cdot 10^{-10})P^6 \\
 &\quad - (2.9466 \cdot 10^{-7})P^5 + (4.781 \cdot 10^{-5})P^4 \\
 &\quad - 0.0039836P^3 + 0.0072596P^2 + 36.75P + 1257.9 \quad (\text{B.3})
 \end{aligned}$$

$$\begin{aligned}
 T_{\text{liq,bas}}(P)[K] &= (1.3728 \cdot 10^{-10})P^6 - (3.7739 \cdot 10^{-8})P^5 \\
 &\quad - (5.0861 \cdot 10^{-7})P^4 + 0.0011277P^3 \\
 &\quad - 0.15346P^2 + 23.869P + 2854.0 \quad (\text{B.4})
 \end{aligned}$$

### Appendix B.2. Pyrolite melting

The solidus function for pyrolite has been taken from Hirschmann (2000) and it is given as:

$$T_{\text{sol,pyr}}(P)[K] = \begin{cases} 273.15 + 1120.661 + 132.899P - 5.104P^2, & \text{if } P < 10 \\ 273.15 + 1939.251 + 30.819(P - 10), & \text{if } P \geq 10 \end{cases} \quad (\text{B.5})$$

The liquidus for pyrolite is an ad hoc compromise between Zerr et al. (1998); Stixrude et al. (2009); Andrault et al. (2011) and it depends on depth as:

$$T_{\text{liq,pyr}}(d)[K] = \begin{cases} 5150 + 0.58d + 3750 \left( \text{erf} \left( \frac{d}{8000} \right) - 1 \right), & \text{for } d > 2900 \\ 2870 + 0.58d + 2800 \left( \text{erf} \left( \frac{d}{800} \right) - 1 \right), & \text{for } d > 660 \\ 2170 + 0.60d + 200 \left( \text{erf} \left( \frac{d}{220} \right) - 1 \right), & \text{for } d < 660 \end{cases} \quad (\text{B.6})$$

### Appendix C. P-T conditions for TTG formation

The amount of TTG produced by partially melting hydrated basalt is computed using the solidus and liquidus temperatures presented in Appendix B. Yet, TTG melts are only formed in

Table D.5: First set of simulations with coesite-stishovite phase transition, initial core temperature  $T_{\text{cmb}} = 6000\text{ K}$ , friction coefficient  $\mu = 0.2$ , depletion fraction  $X_{\text{depletion}}$ , eruption efficiency  $e$  (%), final model runtime  $t_r$  (Gyr), volume of TTG crust  $V_{\text{TTG,crustal}}$ , volume of basaltic crust  $V_{\text{bas,crustal}}$ , and volume of total TTG produced  $V_{\text{TTG,total}}$ . All volumes reported here are in  $\text{km}^3$  and at final model runtime.

$X_{\text{depletion}}$	$e$	$t_r$	$V_{\text{TTG,crustal}}$	$V_{\text{bas,crustal}}$	$V_{\text{TTG,total}}$
0.5	10	4.34	$7.44 \cdot 10^{10}$	$1.11 \cdot 10^{10}$	$1.09 \cdot 10^{11}$
0.5	20	0.85	$2.26 \cdot 10^{10}$	$8.12 \cdot 10^9$	$9.84 \cdot 10^{10}$
0.5	30	3.13	$4.10 \cdot 10^{10}$	$9.81 \cdot 10^9$	$1.15 \cdot 10^{11}$
0.5	40	0.38	$3.34 \cdot 10^9$	$5.31 \cdot 10^9$	$5.23 \cdot 10^{10}$
0.5	60	4.50	$3.42 \cdot 10^{10}$	$8.82 \cdot 10^9$	$1.18 \cdot 10^{11}$
0.5	80	1.01	$1.02 \cdot 10^{10}$	$7.29 \cdot 10^9$	$8.63 \cdot 10^{10}$
0.5	100	4.50	$2.53 \cdot 10^{10}$	$9.29 \cdot 10^9$	$9.97 \cdot 10^{10}$
0.9	10	1.58	$5.02 \cdot 10^9$	$6.73 \cdot 10^9$	$2.43 \cdot 10^{10}$
0.9	20	3.15	$2.49 \cdot 10^9$	$6.43 \cdot 10^9$	$2.91 \cdot 10^{10}$
0.9	30	0.23	$1.56 \cdot 10^9$	$5.07 \cdot 10^9$	$1.26 \cdot 10^{10}$
0.9 <sup>a</sup>	40	4.41	$1.43 \cdot 10^9$	$4.41 \cdot 10^9$	$3.12 \cdot 10^{10}$
0.9	60	0.34	$1.20 \cdot 10^9$	$3.97 \cdot 10^9$	$1.85 \cdot 10^{10}$
0.9	80	3.23	$1.29 \cdot 10^9$	$4.80 \cdot 10^9$	$2.94 \cdot 10^{10}$
0.9	100	1.25	$1.69 \cdot 10^9$	$4.27 \cdot 10^9$	$2.28 \cdot 10^{10}$

<sup>a</sup> simulation *e40x9* presented in Fig. 6 and 7

the pressure-temperature range presented in Fig. 2 and this Appendix. In the present study, we consider that basalt simply forms molten basalt if the P-T conditions for TTG formation are not met.

Following the parameterisation of Rozel et al. (2017) (based on Moyen (2011)), low and medium pressure TTGs form from hydrated basalt in the following conditions (T is in  $^{\circ}\text{C}$  and P is in GPa):

$$760 - 60(P - 1)^2 < T < 1000 - 150\left(\frac{P - 1.2}{1.2}\right)^2 \quad (\text{C.1})$$

$$-0.5\left(\frac{T - 870}{220}\right) < P < 1.5 + 0.7\left(\frac{T - 700}{200}\right), \quad (\text{C.2})$$

where low pressure TTGs form at pressures lower than 1 GPa and medium pressure form above 1 GPa. Additionally, high pressure TTG rocks form under these conditions:

$$1000 < T < 1100 + 50\left(\frac{P - 3.5}{3.5}\right)^2 \quad (\text{C.3})$$

$$2.35 + 0.15\left(\frac{T - 1000}{100}\right) < P < 5. \quad (\text{C.4})$$

#### Appendix D. Volumes at final model runtime

#### Appendix E. Empirical fits for total and crustal TTG production

Table E.7 shows empirical fits of volumes of total TTG produced  $V_{\text{TTG,total}}$  and TTG crust remaining at the surface  $V_{\text{TTG,crustal}}$ . Since in both cases we observe a two-stage growth, we

Table D.6: Second set of simulations with depletion fraction  $X_{\text{depletion}} = 0.5$ , core temperature  $T_{\text{cmb}}$  (K), friction coefficient  $\mu$ , eruption efficiency  $e$  (%), final model runtime  $t_r$  (Gyr), volume of TTG crust  $V_{\text{TTG,crustal}}$ , volume of basaltic crust  $V_{\text{bas,crustal}}$ , and volume of total TTG produced  $V_{\text{TTG,total}}$ . All volumes reported here are in  $\text{km}^3$  and at final model runtime.

$T_{\text{cmb}}$	$\mu$	$e$	$t_r$	$V_{\text{TTG,crustal}}$	$V_{\text{bas,crustal}}$	$V_{\text{TTG,total}}$
5000	0.2	10	1.82	$4.19 \cdot 10^{10}$	$1.16 \cdot 10^{10}$	$9.43 \cdot 10^{10}$
5000	0.2	20	0.88	$1.23 \cdot 10^{10}$	$5.94 \cdot 10^9$	$6.37 \cdot 10^{10}$
5000	0.2	30	3.81	$3.04 \cdot 10^{10}$	$9.40 \cdot 10^9$	$9.57 \cdot 10^{10}$
5000	0.2	40	2.28	$2.20 \cdot 10^{10}$	$9.86 \cdot 10^9$	$8.17 \cdot 10^{10}$
5000 <sup>x</sup>	0.2	60	2.74	$1.78 \cdot 10^{10}$	$1.05 \cdot 10^{10}$	$8.16 \cdot 10^{10}$
5000	0.2	80	0.43	$1.92 \cdot 10^9$	$4.37 \cdot 10^9$	$3.01 \cdot 10^{10}$
5000	0.2	100	4.28	$1.77 \cdot 10^{10}$	$7.17 \cdot 10^9$	$7.68 \cdot 10^{10}$
6000	0.2	10	2.78	$4.89 \cdot 10^{10}$	$1.04 \cdot 10^{10}$	$1.10 \cdot 10^{11}$
6000	0.2	20	2.60	$4.49 \cdot 10^{10}$	$1.06 \cdot 10^{10}$	$1.09 \cdot 10^{11}$
6000 <sup>b</sup>	0.2	30	4.31	$4.30 \cdot 10^{10}$	$1.06 \cdot 10^{10}$	$1.10 \cdot 10^{11}$
6000	0.2	40	3.11	$3.24 \cdot 10^{10}$	$1.06 \cdot 10^{10}$	$1.02 \cdot 10^{11}$
6000	0.2	60	2.70	$2.54 \cdot 10^{10}$	$9.89 \cdot 10^9$	$9.77 \cdot 10^{10}$
6000	0.2	80	4.50	$2.22 \cdot 10^{10}$	$1.04 \cdot 10^{10}$	$9.32 \cdot 10^{10}$
6000	0.2	100	4.50	$2.41 \cdot 10^{10}$	$1.09 \cdot 10^{10}$	$8.73 \cdot 10^{10}$
6000	0.4	10	2.50	$5.53 \cdot 10^{10}$	$1.30 \cdot 10^{10}$	$1.09 \cdot 10^{11}$
6000 <sup>x</sup>	0.4	20	1.70	$3.21 \cdot 10^{10}$	$1.09 \cdot 10^{10}$	$1.03 \cdot 10^{11}$
6000	0.4	30	1.29	$2.57 \cdot 10^{10}$	$1.01 \cdot 10^{10}$	$8.96 \cdot 10^{10}$
6000	0.4	40	2.47	$2.96 \cdot 10^{10}$	$1.04 \cdot 10^{10}$	$1.00 \cdot 10^{11}$
6000	0.4	60	1.58	$1.63 \cdot 10^{10}$	$1.02 \cdot 10^{10}$	$8.46 \cdot 10^{10}$
6000	0.4	80	4.39	$2.39 \cdot 10^{10}$	$1.06 \cdot 10^{10}$	$9.20 \cdot 10^{10}$
6000	0.4	100	4.50	$2.83 \cdot 10^{10}$	$1.17 \cdot 10^{10}$	$9.01 \cdot 10^{10}$

<sup>b</sup> simulation *e30x5* presented in Fig. 8, 9 and 10

<sup>x</sup> excluded from empirical fits owing to data corruption

Table E.7: Empirical fits of the volume of TTG rocks as a function of time. Two stages are observed for both cases: total TTG production and TTG crust.

A - Total TTG volume produced, early stages		Stand. Dev.
$V_{\text{TTG,total}}$	$= 10^{10} A_0 (t - t_0)^{0.929}$	$2.43 \cdot 10^9$
$A_0$	$= 10.047 - 1.339 \frac{e}{50}$	
$t_0$	$= 1.076 - 1.227 \frac{T_{\text{cmb}}}{6000}$	
B - Total TTG volume produced, late stages		Stand. Dev.
$V_{\text{TTG,total}}$	$= 10^{10} (A_0(t_1 - t_0)^{0.929} + 3.432 (t - t_1)^{0.281})$	$2.38 \cdot 10^9$
$t_1$	$= 0.552 - 0.0884 \frac{e}{50}$	
C - TTG crust volume, early stages		Stand. Dev.
$V_{\text{TTG,crustal}}$	$= 10^{10} (0.213 + A_1 t^{2.319})$	$6.86 \cdot 10^8$
$A_1$	$= \max(-7.320 + 4.839 \exp(-1.512 \frac{e}{50}) + 7.536 \frac{T_{\text{cmb}}}{6000}, 0)$	
D - TTG crust volume, late stages		Stand. Dev.
$V_{\text{TTG,crustal}}$	$= 10^{10} (0.213 + A_1 t_2^{2.319} + 0.934 (t - t_2)^{0.639})$	$2.97 \cdot 10^9$
$t_2$	$= 1.021 - 0.108 \frac{e}{50}$	

performed scalings for “early stages”, between 4.25-3.75 Ga, and “late stages” after 3.5 Ga. Fig. E.15 represents the TTG volume generated in all our simulations (y-axis) as a function of our empirical fits (x-axis). All numbers presented in Table E.7 have been obtained by automated search of the possible combinations giving the lowest misfit. Scalings were done only for the second set of simulations presented in Table 4.

#### Appendix E.1. Volume of total TTG produced

TTG production only starts when the first plumes arrive at the surface. Yet, we did not attempt to perform an estimation of the plume arrival time as our initial state might be unrealistic. The arrival time of plumes depends on the time of growth of thermal boundary layer at the core-mantle boundary and the transit time of Earth’s mantle (time taken by a plume to reach the surface). In the Earth, very vigorous solid-state convection probably started during crystallisation of the magma ocean, which is unfortunately very hard to simulate numerically. Starting from a very smooth state (boundary layers superimposed on an adiabatic temperature profile), we know that the timing of plume arrival has very little physical meaning.

When the plumes arrive at the surface, we observe a very strong TTG production rate. Table E.7A shows that the growth is almost linear with time (exponent 0.929). The growth prefactor depends on the eruption efficiency: high eruption efficiency can decrease the TTG production by up to 25%. An origin time  $t_0$  is found that depends on the initial core temperature, with higher temperature resulting in smaller origin time. Although this makes sense from a dynamical point of view, we believe that this observation might be strongly based on our over-simplified initial condition. Interestingly, we found that the core temperature has a negligible effect on the growth rate of TTG. This makes sense as plumes are not controlling the vertical temperature gradient

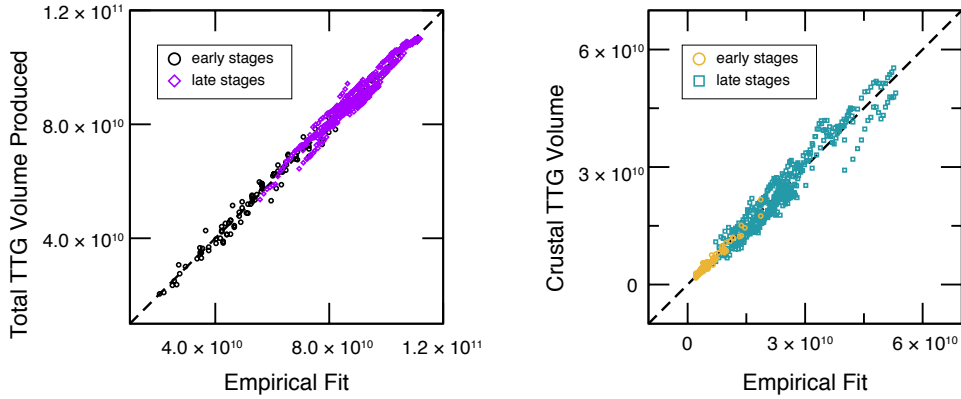


Figure E.15: Total TTG production (*left*) and TTG crust volume (*right*). One point per hundred million years have been extracted from the curves represented in Fig. 11C and 12A for all simulations. Numerical results are presented in the y-axis, empirical fits are shown on the x-axis. Empirical fits for early stages (black and yellow circles) and late stages (light purple diamonds and cyan squares) are represented separately (see Table E.7 for their expressions).

responsible for TTG formation conditions, whereas the eruption efficiency strongly impacts the geotherm.

From Table E.7B, Fig. 11C and 12A, we can see that TTG production decreases drastically around 3.8-3.6 Ga. The growth curve suddenly follows a cubic root of time (exponent 0.281) and has not been found to depend on initial core temperature or eruption efficiency. The inflection time  $t_i$  at which growth slows down is different from the time  $t_1$  presented in Table E.7:  $t_1$  represents the origin of the time-root. Yet, we can see on Fig. 11C and 12A that the inflection time depends on the eruption efficiency: TTG production slows down quickly for simulations with high eruption efficiency than for the ones with intrusive magmatism. After the inflection, the simplicity of the TTG production rate is remarkable and surprising. No matter what happened in the first billion years of evolution, TTG production slows down and proceeds at the exact same rate for all simulations. Such a drop in crust production rate is usually interpreted as the onset of subduction-driven plate tectonics (e.g., Cawood et al., 2006; Shirey and Richardson, 2011; Dhuime et al., 2012; Hawkesworth et al., 2016, 2017). However, we find here that TTG production can suddenly decrease without a significant change in the convection regime owing to mantle depletion as mentioned in Section 4.1.

#### Appendix E.2. Volume of TTG crust

The volume of TTG crust remaining at the surface in our simulations follows a very different trend than the total TTG production itself. Fig. 11C and 12A show that a volume of TTG appears with the arrival of the first plumes. This initial volume seems to not depend on the eruption efficiency, except for the extremely low values of  $e$  (see yellow curves). Table E.7C shows that a quasi-parabolic growth follows for about 1 billion years (exponent 2.319). Both initial core temperature and eruption efficiency have an influence on this growth rate. In particular, cases with

Table F.8: Final masses of each type of TTG produced for the first set of simulations with coesite-stishovite phase transition, initial core temperature  $T_{\text{cmb}} = 6000 \text{ K}$ , friction coefficient  $\mu = 0.2$ , depletion fraction  $X_{\text{depletion}}$ , eruption efficiency  $e$  (%), final model runtime  $t_r$  (Gyr), mass of low-pressure TTG  $M_{\text{TTG,LP}}$ , mass of medium-pressure TTG  $M_{\text{TTG,MP}}$ , mass of high-pressure TTG  $M_{\text{TTG,HP}}$ , and mass of total TTG  $M_{\text{TTG,total}}$ . All masses reported here are in kg and at final model runtime.

$X_{\text{depletion}}$	$e$	$t_r$	$M_{\text{TTG,LP}}$	$M_{\text{TTG,MP}}$	$M_{\text{TTG,HP}}$	$M_{\text{TTG,total}}$
0.5	10	4.34	$6.17 \cdot 10^{20}$	$2.20 \cdot 10^{20}$	$6.55 \cdot 10^{19}$	$9.03 \cdot 10^{20}$
0.5	20	0.85	$5.95 \cdot 10^{20}$	$2.01 \cdot 10^{20}$	$1.86 \cdot 10^{19}$	$8.15 \cdot 10^{20}$
0.5	30	3.13	$6.81 \cdot 10^{20}$	$2.44 \cdot 10^{20}$	$2.64 \cdot 10^{19}$	$9.51 \cdot 10^{20}$
0.5	40	0.38	$3.20 \cdot 10^{20}$	$1.07 \cdot 10^{20}$	$5.96 \cdot 10^{18}$	$4.33 \cdot 10^{20}$
0.5	60	4.50	$6.94 \cdot 10^{20}$	$2.57 \cdot 10^{20}$	$2.38 \cdot 10^{19}$	$9.74 \cdot 10^{20}$
0.5	80	1.01	$5.15 \cdot 10^{20}$	$1.88 \cdot 10^{20}$	$1.14 \cdot 10^{19}$	$7.15 \cdot 10^{20}$
0.5	100	4.50	$6.17 \cdot 10^{20}$	$1.96 \cdot 10^{20}$	$1.25 \cdot 10^{19}$	$8.26 \cdot 10^{20}$
0.9	10	1.58	$1.76 \cdot 10^{20}$	$2.45 \cdot 10^{19}$	$9.09 \cdot 10^{17}$	$2.01 \cdot 10^{20}$
0.9	20	3.15	$2.07 \cdot 10^{20}$	$3.24 \cdot 10^{19}$	$1.12 \cdot 10^{18}$	$2.41 \cdot 10^{20}$
0.9	30	0.23	$9.33 \cdot 10^{19}$	$1.10 \cdot 10^{19}$	$3.27 \cdot 10^{17}$	$1.05 \cdot 10^{20}$
0.9 <sup>a</sup>	40	4.41	$2.18 \cdot 10^{20}$	$3.96 \cdot 10^{19}$	$1.41 \cdot 10^{18}$	$2.59 \cdot 10^{20}$
0.9	60	0.34	$1.35 \cdot 10^{20}$	$1.83 \cdot 10^{19}$	$7.32 \cdot 10^{17}$	$1.54 \cdot 10^{20}$
0.9	80	3.23	$2.05 \cdot 10^{20}$	$3.64 \cdot 10^{19}$	$1.54 \cdot 10^{18}$	$2.43 \cdot 10^{20}$
0.9	100	1.25	$1.60 \cdot 10^{20}$	$2.81 \cdot 10^{19}$	$1.19 \cdot 10^{18}$	$1.89 \cdot 10^{20}$

<sup>a</sup> simulation *e40x9* presented in Fig. 6 and 7

low eruption efficiency generate up to 3 times more TTG rocks compared to eruptive cases. TTG production is slightly smaller for cases with lower initial core temperature, but the governing parameter here seems to be the eruption efficiency.

A late growth phase of TTG crust starts after 3.5-3.1 Ga. Table E.7D shows that all curves then follow a simple trend following a quasi square root of time (exponent 0.639). Similar to the total TTG production, this shows that crustal growth does not depend on the initial core temperature or eruption efficiency in the “late stages”. It seems that the most important contribution comes from the initial stages of production, and growth slows down at the inflection point, even though plate tectonics do not start.

## Appendix F. TTG type at final model runtime

### Acknowledgments

We thank Peter Cawood and Nicolas Flament for their constructive feedback during the review process that helped improve the manuscript, and Nicholas Rawlinson for his editorial work. C. Jain and A. B. Rozel received funding from the European Research Council under the European Union’s Seventh Framework Programme (FP/20072013)/ERC Grant Agreement number 320639 project iGEO. P. Sanan acknowledges financial support from the Swiss University Conference and the Swiss Council of Federal Institutes of Technology through the Platform for Advanced Scientific Computing (PASC) program. The perceptually-uniform colour maps are used in this study to prevent visual distortion of the data (Crameri, 2018b,a).

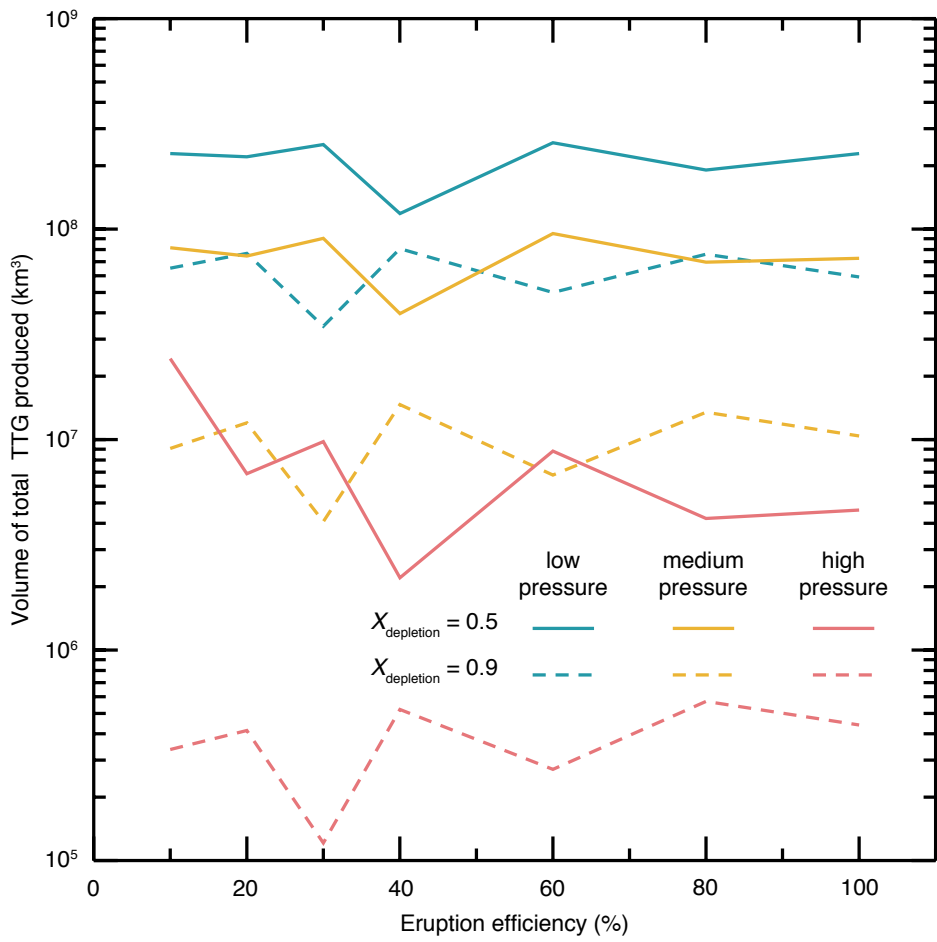


Figure F.16: Final volumes of each type of TTG produced for the first set of simulations presented in Table 3 with depletion fraction  $X_{\text{depletion}} = 0.5$  (solid lines) and 0.9 (dashed lines).

Table F.9: Final masses of each type of TTG produced for the second set of simulations with depletion fraction  $X_{\text{depletion}} = 0.5$ , core temperature  $T_{\text{cmb}}$  (K), friction coefficient  $\mu$ , eruption efficiency  $e$  (%), final model runtime  $t_r$  (Gyr), mass of low-pressure TTG  $M_{\text{TTG,LP}}$ , mass of medium-pressure TTG  $M_{\text{TTG,MP}}$ , mass of high-pressure TTG  $M_{\text{TTG,HP}}$ , and mass of total TTG  $M_{\text{TTG,total}}$ . All masses reported here are in kg and at final model runtime.

$T_{\text{cmb}}$	$\mu$	$e$	$t_r$	$M_{\text{TTG,LP}}$	$M_{\text{TTG,MP}}$	$M_{\text{TTG,HP}}$	$M_{\text{TTG,total}}$
5000	0.2	10	1.82	$3.97 \cdot 10^{20}$	$3.53 \cdot 10^{20}$	$3.27 \cdot 10^{19}$	$7.83 \cdot 10^{20}$
5000	0.2	20	0.88	$2.79 \cdot 10^{20}$	$2.63 \cdot 10^{20}$	$9.35 \cdot 10^{18}$	$5.50 \cdot 10^{20}$
5000	0.2	30	3.81	$3.96 \cdot 10^{20}$	$3.70 \cdot 10^{20}$	$2.71 \cdot 10^{19}$	$7.93 \cdot 10^{20}$
5000	0.2	40	2.28	$3.26 \cdot 10^{20}$	$3.43 \cdot 10^{20}$	$1.38 \cdot 10^{19}$	$6.82 \cdot 10^{20}$
5000 <sup>x</sup>	0.2	60	2.74	$3.14 \cdot 10^{20}$	$3.52 \cdot 10^{20}$	$1.28 \cdot 10^{19}$	$6.79 \cdot 10^{20}$
5000	0.2	80	0.43	$1.25 \cdot 10^{20}$	$1.34 \cdot 10^{20}$	$2.98 \cdot 10^{18}$	$2.62 \cdot 10^{20}$
5000	0.2	100	4.28	$2.81 \cdot 10^{20}$	$3.46 \cdot 10^{20}$	$1.06 \cdot 10^{19}$	$6.38 \cdot 10^{20}$
6000	0.2	10	2.78	$4.43 \cdot 10^{20}$	$4.16 \cdot 10^{20}$	$5.40 \cdot 10^{19}$	$9.13 \cdot 10^{20}$
6000	0.2	20	2.60	$4.40 \cdot 10^{20}$	$4.18 \cdot 10^{20}$	$4.53 \cdot 10^{19}$	$9.03 \cdot 10^{20}$
6000 <sup>b</sup>	0.2	30	4.31	$4.33 \cdot 10^{20}$	$4.31 \cdot 10^{20}$	$4.99 \cdot 10^{19}$	$9.14 \cdot 10^{20}$
6000	0.2	40	3.11	$4.00 \cdot 10^{20}$	$4.11 \cdot 10^{20}$	$3.43 \cdot 10^{19}$	$8.45 \cdot 10^{20}$
6000	0.2	60	2.70	$3.66 \cdot 10^{20}$	$4.24 \cdot 10^{20}$	$2.22 \cdot 10^{19}$	$8.13 \cdot 10^{20}$
6000	0.2	80	4.50	$3.39 \cdot 10^{20}$	$4.07 \cdot 10^{20}$	$2.58 \cdot 10^{19}$	$7.72 \cdot 10^{20}$
6000	0.2	100	4.50	$3.19 \cdot 10^{20}$	$3.87 \cdot 10^{20}$	$1.67 \cdot 10^{19}$	$7.23 \cdot 10^{20}$
6000	0.4	10	2.50	$4.49 \cdot 10^{20}$	$3.98 \cdot 10^{20}$	$5.91 \cdot 10^{19}$	$9.06 \cdot 10^{20}$
6000 <sup>x</sup>	0.4	20	1.70	$4.32 \cdot 10^{20}$	$3.95 \cdot 10^{20}$	$3.39 \cdot 10^{19}$	$8.61 \cdot 10^{20}$
6000	0.4	30	1.29	$3.57 \cdot 10^{20}$	$3.76 \cdot 10^{20}$	$2.54 \cdot 10^{19}$	$7.58 \cdot 10^{20}$
6000	0.4	40	2.47	$3.94 \cdot 10^{20}$	$4.14 \cdot 10^{20}$	$2.75 \cdot 10^{19}$	$8.35 \cdot 10^{20}$
6000	0.4	60	1.58	$3.15 \cdot 10^{20}$	$3.75 \cdot 10^{20}$	$1.80 \cdot 10^{19}$	$7.08 \cdot 10^{20}$
6000	0.4	80	4.39	$3.45 \cdot 10^{20}$	$4.01 \cdot 10^{20}$	$2.23 \cdot 10^{19}$	$7.69 \cdot 10^{20}$
6000	0.4	100	4.50	$3.23 \cdot 10^{20}$	$4.03 \cdot 10^{20}$	$2.00 \cdot 10^{19}$	$7.46 \cdot 10^{20}$

<sup>b</sup> simulation *e30x5* presented in Fig. 8, 9 and 10

<sup>x</sup> excluded from empirical fits owing to data corruption

## References

- Akaogi, M., Navrotsky, A., 1984. The quartz-coesite-stishovite transformations: new calorimetric measurements and calculation of phase diagrams. *Physics of the Earth and Planetary Interiors* 36, 124–134.
- Akimoto, S.i., Syono, Y., 1969. Coesite-Stishovite transition. *Journal of Geophysical Research* 74, 1653–1659.
- Albarède, F., 1998. The growth of continental crust. *Tectonophysics* 296, 1–14.
- Allègre, C.J., Rousseau, D., 1984. The growth of the continent through geological time studied by Nd isotope analysis of shales. *Earth and Planetary Science Letters* 67, 19–34.
- Amestoy, P.R., Duff, I.S., L'Excellent, J.Y., 2000. Multifrontal parallel distributed symmetric and unsymmetric solvers. *Computer Methods in Applied Mechanics and Engineering* 184, 501–520.
- Ammann, M.W., Brodholt, J.P., Wookey, J., Dobson, D.P., 2010. First-principles constraints on diffusion in lower-mantle minerals and a weak D'' layer. *Nature* 465, 462–465.
- Andrault, D., Bolfan-Casanova, N., Lo Nigro, G., Bouhifd, M.A., Garbarino, G., Mezouar, M., 2011. Solidus and liquidus profiles of chondritic mantle: Implication for melting of the Earth across its history. *Earth and Planetary Science Letters* 304, 251–259.
- Andrault, D., Pesce, G., Bouhifd, M.A., Bolfan-Casanova, N., Henot, J.M., Mezouar, M., 2014. Melting of subducted basalt at the core-mantle boundary. *Science* 344, 892–895.
- Arculus, R.J., 1999. Origins of the continental crust. *Journal and Proceedings of the Royal Society of New South Wales*.
- Armstrong, R.L., 1981. Radiogenic Isotopes: The Case for Crustal Recycling on a Near-Steady-State No-Continental-Growth Earth. *Philosophical Transactions of the Royal Society of London Series A: Mathematical Physical and Engineering Sciences* 301, 443–472.
- Armstrong, R.L., 1991. The persistent myth of crustal growth. *Australian Journal of Earth Sciences* 38, 613–630.
- Arndt, N., 2013. Formation and Evolution of the Continental Crust. *Geochemical Perspectives* 2, 405–533.
- Arndt, N.T., Coltice, N., Helmstaedt, H., Gregoire, M., 2009. Origin of Archean subcontinental lithospheric mantle: Some petrological constraints. *LITHOS* 109, 61–71.
- Atherton, M.P., Petford, N., 1993. Generation of sodium-rich magmas from newly underplated basaltic crust. *Nature* 362, 144–146.
- Balay, S., Abhyankar, S., Adams, M.F., Brown, J., Brune, P., Buschelman, K., Dalcin, L., Eijkhout, V., Gropp, W.D., Kaushik, D., Knepley, M.G., May, D.A., McInnes, L.C., Mills, R.T., Munson, T., Rupp, K., Sanan, P., Smith, B.F., Zampini, S., Zhang, H., Zhang, H., 2018a. PETSc Web page. URL: <http://www.mcs.anl.gov/petsc>.
- Balay, S., Abhyankar, S., Adams, M.F., Brown, J., Brune, P., Buschelman, K., Dalcin, L., Eijkhout, V., Gropp, W.D., Kaushik, D., Knepley, M.G., May, D.A., McInnes, L.C., Mills, R.T., Munson, T., Rupp, K., Sanan, P., Smith, B.F., Zampini, S., Zhang, H., Zhang, H., 2018b. PETSc Users Manual. Technical Report ANL-95/11 - Revision 3.9. Argonne National Laboratory. URL: <http://www.mcs.anl.gov/petsc>.
- Barker, F., Arth, J.G., 1976. Generation of trondhjemitic-tonalitic liquids and Archean bimodal trondhjemite-basalt suites. *Geology* 4, 596.
- Barth, M.G., McDonough, W.F., Rudnick, R.L., 2000. Tracking the budget of Nb and Ta in the continental crust. *Chemical geology* 165, 197–213.
- Beall, A.P., Moresi, L., Cooper, C.M., 2018. Formation of cratonic lithosphere during the initiation of plate tectonics. *Geology* 46, 487–490.
- Bédard, J.H., 2006. A catalytic delamination-driven model for coupled genesis of Archean crust and sub-continental lithospheric mantle. *GEOCHIMICA ET COSMOCHIMICA ACTA* 70, 1188–1214.
- Bédard, J.H., Harris, L.B., Thurston, P.C., 2013. The hunting of the Arc. *Precambrian research* 229, 20–48.
- Belousova, E.A., Kostitsyn, Y.A., Griffin, W.L., Begg, G.C., O'Reilly, S.Y., Pearson, N.J., 2010. The growth of the continental crust: Constraints from zircon Hf-isotope data. *LITHOS* 119, 457–466.
- Brown, M., 2006. Duality of thermal regimes is the distinctive characteristic of plate tectonics since the Neoproterozoic. *Geology* 34, 961.
- Buffett, B.A., Huppert, H.E., Lister, J.R., Woods, A.W., 1992. Analytical Model for Solidification of the Earth's Core. *Nature* 356, 329–331.
- Buffett, B.A., Huppert, H.E., Lister, J.R., Woods, A.W., 1996. On the thermal evolution of the Earth's core. *Journal of Geophysical Research* 101, 7989–8006.
- Byerlee, J., 1978. Friction of Rocks. *Pure and Applied Geophysics* 116, 615–626.
- Campbell, I.H., Allen, C.M., 2008. Formation of supercontinents linked to increases in atmospheric oxygen. *Nature Geoscience* 1, 554–558.
- Cawood, P.A., Hawkesworth, C.J., Dhuime, B., 2013. The continental record and the generation of continental crust. *Geological Society of America Bulletin* 125, 14–32.
- Cawood, P.A., Kröner, A., Pisarevsky, S., 2006. Precambrian plate tectonics: Criteria and evidence. *GSA Today* 16, 4.
- Chowdhury, P., Gerya, T., Chakraborty, S., 2017. Emergence of silicic continents as the lower crust peels off on a hot plate-tectonic Earth. *Nature Geoscience* 10, 698–703.

- Christensen, U.R., Hofmann, A.W., 1994. Segregation of subducted oceanic crust in the convecting mantle. *Journal of Geophysical Research* 99, 19867–19884.
- Čížková, H., van den Berg, A.P., Spakman, W., Matyska, C., 2012. The viscosity of Earth's lower mantle inferred from sinking speed of subducted lithosphere. *Physics of the Earth and Planetary Interiors* 200–201, 56–62.
- Condie, K.C., 1986. Origin and Early Growth-Rate of Continents. *Precambrian Research* 32, 261–278.
- Condie, K.C., 1998. Episodic continental growth and supercontinents: a mantle avalanche connection? *Earth and Planetary Science Letters* 163, 97–108.
- Condie, K.C., 2000. Episodic continental growth models: afterthoughts and extensions. *Tectonophysics* 322, 153–162.
- Condie, K.C., 2004. Supercontinents and superplume events: distinguishing signals in the geologic record. *Physics of the Earth and Planetary Interiors* 146, 319–332.
- Condie, K.C., 2018. A planet in transition: The onset of plate tectonics on Earth between 3 and 2 Ga? *Geoscience Frontiers* 9, 51–60.
- Condie, K.C., Aster, R.C., 2010. Episodic zircon age spectra of orogenic granitoids: The supercontinent connection and continental growth. *Precambrian research* 180, 227–236.
- Condie, K.C., Aster, R.C., van Hunen, J., 2016. A great thermal divergence in the mantle beginning 2.5 Ga: Geochemical constraints from greenstone basalts and komatiites. *Geoscience Frontiers* 7, 543–553.
- Condie, K.C., Kröner, A., 2008. When did plate tectonics begin? Evidence from the geologic record, in: *Special Paper 440: When Did Plate Tectonics Begin on Planet Earth?*. Geological Society of America, pp. 281–294.
- Crameri, F., 2018a. Geodynamic diagnostics, scientific visualisation and StagLab 3.0. *Geoscientific Model Development Discussions*, 1–41.
- Crameri, F., 2018b. Scientific colour maps. URL: <https://doi.org/10.5281/zenodo.1243863>, doi:10.5281/zenodo.1243863. The development of the scientific colour maps is supported by the Research Council of Norway through its Centers of Excellence funding scheme, Project Number 223272.
- Crisp, J.A., 1984. Rates of Magma Emplacement and Volcanic Output. *Journal of Volcanology and Geothermal Research* 20, 177–211.
- Debaille, V., O'Neill, C., Brandon, A.D., Haenecour, P., Yin, Q.Z., Mattielli, N., Treiman, A.H., 2013. Stagnant-lid tectonics in early Earth revealed by 142Nd variations in late Archean rocks. *Earth and Planetary Science Letters* 373, 83–92.
- Dhuime, B., Hawkesworth, C.J., Cawood, P.A., Storey, C.D., 2012. A Change in the Geodynamics of Continental Growth 3 Billion Years Ago. *Science* 335, 1334–1336.
- Dhuime, B., Hawkesworth, C.J., Delavault, H., Cawood, P.A., 2017. Continental growth seen through the sedimentary record. *Sedimentary Geology* 357, 16–32.
- Drummond, M.S., Defant, M.J., 1990. A model for Trondhjemite-Tonalite-Dacite Genesis and crustal growth via slab melting: Archean to modern comparisons. *Journal of Geophysical Research* 95, 21503–21521.
- Fischer, R., Gerya, T., 2016. Early Earth plume-lid tectonics: A high-resolution 3D numerical modelling approach. *Journal of Geodynamics* 100, 198–214.
- Flament, N., Coltice, N., Rey, P.F., 2013. The evolution of the 87Sr/86Sr of marine carbonates does not constrain continental growth. *Precambrian research* 229, 177–188.
- Foley, S., Tiepolo, M., Vannucci, R., 2002. Growth of early continental crust controlled by melting of amphibolite in subduction zones. *Nature* 417, 837–840.
- Foley, S.F., Buhre, S., Jacob, D.E., 2003. Evolution of the Archaean crust by delamination and shallow subduction. *Nature* 421, 249–252.
- François, C., Philippot, P., Rey, P., Rubatto, D., 2014. Burial and exhumation during Archean sagduction in the East Pilbara Granite-Greenstone Terrane. *Earth and Planetary Science Letters* 396, 235–251.
- Gerya, T., 2014. Precambrian geodynamics: Concepts and models. *Gondwana Research* 25, 442–463.
- Gerya, T.V., Maresch, W.V., Podlesskii, K.K., Perchuk, L.L., 2004. Semi-empirical Gibbs free energy formulations for minerals and fluids for use in thermodynamic databases of petrological interest. *Physics and Chemistry of Minerals* 31, 429–455.
- Gerya, T.V., Stern, R.J., Baes, M., Sobolev, S.V., Whattam, S.A., 2015. Plate tectonics on the Earth triggered by plume-induced subduction initiation. *Nature* 527, 221–225.
- Goodwin, A.M., 1991. *Precambrian Geology: the dynamic evolution of the continental crust*. Academic Press Geology Series, Academic Press.
- Gregg, P.M., Behn, M.D., Lin, J., Grove, T.L., 2009. Melt generation, crystallization, and extraction beneath segmented oceanic transform faults. *Journal of Geophysical Research* 114, 115.
- Griffin, W.L., O'Reilly, S.Y., 2007. Cratonic lithospheric mantle: Is anything subducted? *Episodes* 30, 43–53.
- Griffin, W.L., O'Reilly, S.Y., Abe, N., Aulbach, S., Davies, R.M., Pearson, N.J., Doyle, B.J., Kivi, K., 2003. The origin and evolution of Archean lithospheric mantle. *Precambrian Research* 127, 19–41.
- Hastie, A.R., Fitton, J.G., Mitchell, S.F., Neill, I., Nowell, G.M., Millar, I.L., 2015. Can Fractional Crystallization, Mixing and Assimilation Processes be Responsible for Jamaican-type Adakites? Implications for Generating Eoarchaean

- Continental Crust. *Journal of Petrology* 56, 1251–1284.
- Hawkesworth, C.J., Cawood, P.A., Dhuime, B., 2016. Tectonics and crustal evolution. *GSA Today* 26, 4–11.
- Hawkesworth, C.J., Cawood, P.A., Dhuime, B., Kemp, T.I.S., 2017. Earth's Continental Lithosphere Through Time. *Annual Review of Earth and Planetary Sciences* 45, 169–198.
- Hawkesworth, C.J., Kemp, A.I.S., 2006a. Evolution of the continental crust. *Nature* 443, 811–817.
- Hawkesworth, C.J., Kemp, A.I.S., 2006b. The differentiation and rates of generation of the continental crust. *Chemical geology* 226, 134–143.
- Hernlund, J.W., Tackley, P.J., 2008. Modeling mantle convection in the spherical annulus. *Physics of the Earth and Planetary Interiors* 171, 48–54.
- Herzberg, C., Condie, K., Korenaga, J., 2010. Thermal history of the Earth and its petrological expression. *Earth and Planetary Science Letters* 292, 79–88.
- Herzberg, C., Gazel, E., 2009. Petrological evidence for secular cooling in mantle plumes. *Nature* 458, 619–622.
- Herzberg, C.T., 1993. Lithosphere peridotites of the Kaapvaal craton. *Earth and Planetary Science Letters* 120, 13–29.
- Hickman, A.H., 2004. Two contrasting granite-greenstone terranes in the Pilbara Craton, Australia: evidence for vertical and horizontal tectonic regimes prior to 2900Ma. *Precambrian Research* 131, 153–172.
- Hirschmann, M.M., 2000. Mantle solidus: Experimental constraints and the effects of peridotite composition. *Geochemistry, Geophysics, Geosystems* 1.
- Hoffmann, P.F., 1989. Precambrian geology and tectonic history of North America. *Geology of North America—An Overview*, Geological Society of America.
- Hofmann, A.W., 1988. Chemical Differentiation of the Earth - the Relationship Between Mantle, Continental-Crust, and Oceanic-Crust. *Earth and Planetary Science Letters* 90, 297–314.
- Hopkins, M., Harrison, T.M., Manning, C.E., 2008. Low heat flow inferred from  $\epsilon$  4 Gyr zircons suggests Hadean plate boundary interactions. *Nature* 456, 493–496.
- Hopkins, M.D., Harrison, T.M., Manning, C.E., 2010. Constraints on Hadean geodynamics from mineral inclusions in  $>4$ Ga zircons. *Earth and Planetary Science Letters* 298, 367–376.
- Huang, Y., Chubakov, V., Mantovani, F., Rudnick, R.L., McDonough, W.F., 2013. A reference Earth model for the heat-producing elements and associated geoneutrino flux. *Geochemistry, Geophysics, Geosystems* 14, 2003–2029.
- van Hunen, J., van Keken, P.E., Hynes, A., Davies, G.F., 2008. Tectonics of early Earth: Some geodynamic considerations, in: *Special Paper 440: When Did Plate Tectonics Begin on Planet Earth?*. Geological Society of America, pp. 157–171.
- van Hunen, J., Moyen, J.F., 2012. Archean Subduction: Fact or Fiction? *Annual Review of Earth and Planetary Sciences* 40, 195–219.
- Hunt, S.A., Weidner, D.J., Li, L., Wang, L., Walte, N.P., Brodholt, J.P., Dobson, D.P., 2009. Weakening of calcium iridate during its transformation from perovskite to post-perovskite. *Nature Geoscience* 2, 794–797.
- Hurley, P.M., Rand, J.R., 1969. Pre-Drift Continental Nuclei. *Science* 164, 1229–1242.
- Irfune, T., Ringwood, A.E., 1993. Phase-Transformations in Subducted Oceanic-Crust and Buoyancy Relationships at Depths of 600–800 Km in the Mantle. *Earth and Planetary Science Letters* 117, 101–110.
- Jahn, B.M., Glikson, A.Y., Peucat, J.J., Hickman, A.H., 1981. REE geochemistry and isotopic data of Archean silicic volcanics and granitoids from the Pilbara Block, Western Australia: implications for the early crustal evolution. *Geochimica et Cosmochimica Acta* 45, 1633–1652.
- Johnson, T.E., Brown, M., Gardiner, N.J., Kirkland, C.L., Smithies, R.H., 2017. Earth's first stable continents did not form by subduction. *Nature* 543, 239–242.
- Johnson, T.E., Brown, M., Kaus, B.J.P., VanTongeren, J.A., 2013a. Delamination and recycling of Archaean crust caused by gravitational instabilities. *Nature Geoscience* 7, 47–52.
- Johnson, T.E., Fischer, S., White, R.W., 2013b. Field and petrographic evidence for partial melting of TTG gneisses from the central region of the mainland Lewisian complex, NW Scotland. *Journal of the Geological Society* 170, 319–326.
- Karato, S.i., Wu, P., 1993. Rheology of the Upper Mantle: A Synthesis. *Science* 260, 771–778.
- Kawai, K., Tsuchiya, T., Tsuchiya, J., Maruyama, S., 2009. Lost primordial continents. *Gondwana Research* 16, 581–586.
- Kemp, A.I.S., Hawkesworth, C.J., 2003. Granitic Perspectives on the Generation and Secular Evolution of the Continental Crust, in: *Treatise on Geochemistry*. Elsevier, pp. 349–410.
- Komabayashi, T., Maruyama, S., Rino, S., 2009. A speculation on the structure of the D'' layer: The growth of anti-crust at the core–mantle boundary through the subduction history of the Earth. *Gondwana Research* 15, 342–353.
- Komiya, T., Maruyama, S., Masuda, T., Nohda, S., Hayashi, M., Okamoto, K., 1999. Plate tectonics at 3.8–3.7 Ga: Field evidence from the Isua Accretionary Complex, southern West Greenland. *Journal of Geology* 107, 515–554.
- Korenaga, J., 2011. Thermal evolution with a hydrating mantle and the initiation of plate tectonics in the early Earth. *Journal of Geophysical Research: Solid Earth* 116.
- Korenaga, J., 2013. Initiation and Evolution of Plate Tectonics on Earth: Theories and Observations. *Annual Review of Earth and Planetary Sciences* 41, 117–151.

- Kusky, T.M., Polat, A., 1999. Growth of granite–greenstone terranes at convergent margins, and stabilization of Archean cratons. *Tectonophysics* 305, 43–73.
- Labrosse, S., Jaupart, C., 2007. Thermal evolution of the Earth: Secular changes and fluctuations of plate characteristics. *Earth and Planetary Science Letters* 260, 465–481.
- Lee, C.T.A., Luffi, P., Chin, E.J., 2011. Building and Destroying Continental Mantle. *Annual Review of Earth and Planetary Sciences* 39, 59–90.
- Lourenço, D.L., 2017. The influence of melting on the thermo-chemical evolution of rocky planets' interiors. Ph.D. thesis. ETH Zurich. URL: <https://www.research-collection.ethz.ch/handle/20.500.11850/228308>, doi:10.3929/ethz-b-000228308.
- Lourenço, D.L., Rozel, A., Tackley, P.J., 2016. Melting-induced crustal production helps plate tectonics on Earth-like planets. *Earth and Planetary Science Letters* 439, 18–28.
- Martin, H., 1986. Effect of steeper Archean geothermal gradient on geochemistry of subduction-zone magmas. *Geology* 14, 753.
- Martin, H., 1994. Chapter 6 The Archean Grey Gneisses and the Genesis of Continental Crust, in: *Archean Crustal Evolution*. Elsevier, pp. 205–259.
- Martin, H., Moyen, J.F., Guitreau, M., Blichert-Toft, J., Le Pennec, J.L., 2014. Why Archean TTG cannot be generated by MORB melting in subduction zones. *LITHOS* 198-199, 1–13.
- McCulloch, M.T., Bennett, V.C., 1994. Progressive growth of the Earth's continental crust and depleted mantle: Geochemical constraints. *GEOCHIMICA ET COSMOCHIMICA ACTA* 58, 4717–4738.
- Moore, W.B., Webb, A.A.G., 2014. Heat-pipe Earth. *Nature* 501, 501–505.
- Moresi, L., Solomatov, V., 1998. Mantle convection with a brittle lithosphere: thoughts on the global tectonic styles of the Earth and Venus. *Geophysical Journal International* 133, 669–682.
- Moyen, J.F., 2011. The composite Archean grey gneisses: Petrological significance, and evidence for a non-unique tectonic setting for Archean crustal growth. *LITHOS* 123, 21–36.
- Moyen, J.F., Stevens, G., 2006. Experimental constraints on TTG petrogenesis: Implications for Archean geodynamics, in: *Archean Geodynamics and Environments*. American Geophysical Union, Washington, D. C., pp. 149–175.
- Nakagawa, T., Tackley, P.J., 2004. Effects of thermo-chemical mantle convection on the thermal evolution of the Earth's core. *Earth and Planetary Science Letters* 220, 107–119.
- Nakagawa, T., Tackley, P.J., 2012. Influence of magmatism on mantle cooling, surface heat flow and Urey ratio. *Earth and Planetary Science Letters* 329, 1–10.
- Nakagawa, T., Tackley, P.J., Deschamps, F., Connolly, J.A.D., 2010. The influence of MORB and harzburgite composition on thermo-chemical mantle convection in a 3-D spherical shell with self-consistently calculated mineral physics. *Earth and Planetary Science Letters* 296, 403–412.
- Nikolaeva, K., Gerya, T.V., Connolly, J.A.D., 2008. Numerical modelling of crustal growth in intraoceanic volcanic arcs. *Physics of the Earth and Planetary Interiors* 171, 336–356.
- Nisbet, E.G., 1982. The tectonic setting and petrogenesis of komatiites., in: Arndt, N.T., Nisbet, E.G. (Eds.), *Komatiites*. George Allen & Unwin, pp. 501–520.
- Ono, S., Ito, E., Katsura, T., 2001. Mineralogy of subducted basaltic crust (MORB) from 25 to 37 GPa, and chemical heterogeneity of the lower mantle. *Earth and Planetary Science Letters* 190, 57–63.
- Ono, S., Kikegawa, T., Higo, Y., Tange, Y., 2017. Precise determination of the phase boundary between coesite and stishovite in SiO<sub>2</sub>. *Physics of the Earth and Planetary Interiors* 264, 1–6.
- O'Reilly, T.C., Davies, G.F., 1981. Magma transport of heat on Io: A mechanism allowing a thick lithosphere. *Geophysical Research Letters* 8, 313–316.
- Plank, T., 2005. Constraints from thorium/lanthanum on sediment recycling at subduction zones and the evolution of the continents. *Journal of Petrology* 46, 921–944.
- Qian, Q., Hermann, J., 2013. Partial melting of lower crust at 10–15 kbar: constraints on adakite and TTG formation. *Contributions to Mineralogy and Petrology* 165, 1195–1224.
- Rapp, R.P., Shimizu, N., Norman, M.D., 2003. Growth of early continental crust by partial melting of eclogite. *Nature* 425, 605–609.
- Rapp, R.P., Watson, E.B., Miller, C.F., 1991. Partial Melting of Amphibolite Eclogite and the Origin of Archean Trondhjemites and Tonalites. *Precambrian Research* 51, 1–25.
- Ricard, Y., Richards, M., Lithgow-Bertelloni, C., Le Stunff, Y., 1993. A geodynamic model of mantle density heterogeneity. *Journal of Geophysical Research* 98, 21895–21909.
- Ricard, Y., Vigny, C., Froidevaux, C., 1989. Mantle heterogeneities, geoid, and plate motion: A Monte Carlo inversion. *Journal of Geophysical Research* 94, 13739–13754.
- Rino, S., Komiya, T., Windley, B.F., Katayama, I., Motoki, A., Hirata, T., 2004. Major episodic increases of continental crustal growth determined from zircon ages of river sands; implications for mantle overturns in the Early Precambrian. *Physics of the Earth and Planetary Interiors* 146, 369–394.
- Roberts, N.M.W., Spencer, C.J., 2015. The zircon archive of continent formation through time. *Geological Society*,

- London, Special Publications 389, 197–225.
- Rozel, A.B., Golabek, G.J., Jain, C., Tackley, P.J., Gerya, T., 2017. Continental crust formation on early Earth controlled by intrusive magmatism. *Nature* 545, 332–335.
- Rudnick, R.L., 1995. Making Continental-Crust. *Nature* 378, 571–578.
- Rudnick, R.L., Gao, S., 2003. Composition of the Continental Crust, in: *Treatise on Geochemistry*. Elsevier, Amsterdam, pp. 1–64.
- Shirey, S.B., Kamber, B.S., Whitehouse, M.J., Mueller, P.A., Basu, A.R., 2008. A review of the isotopic and trace element evidence for mantle and crustal processes in the Hadean and Archean: Implications for the onset of plate tectonic subduction, in: *Special Paper 440: When Did Plate Tectonics Begin on Planet Earth?*. Geological Society of America, pp. 1–29.
- Shirey, S.B., Richardson, S.H., 2011. Start of the Wilson cycle at 3 Ga shown by diamonds from subcontinental mantle. *Science* 333, 434–436.
- Sizova, E., Gerya, T., Brown, M., Perchuk, L.L., 2010. Subduction styles in the Precambrian: Insight from numerical experiments. *LITHOS* 116, 209–229.
- Sizova, E., Gerya, T., Stuewe, K., Brown, M., 2015. Generation of felsic crust in the Archean: A geodynamic modeling perspective. *Precambrian Research* 271, 198–224.
- Smithies, R.H., 2000. The Archean tonalite–trondhjemite–granodiorite (TTG) series is not an analogue of Cenozoic adakite. *Earth and Planetary Science Letters* 182, 115–125.
- Spencer, C.J., Roberts, N.M.W., Santosh, M., 2017. Growth, destruction, and preservation of Earth's continental crust. *Earth Science Reviews* 172, 87–106.
- Springer, W., Seck, H.A., 1997. Partial fusion of basic granulites at 5 to 15 kbar: Implications for the origin of TTG magmas. *Contributions to Mineralogy and Petrology* 127, 30–45.
- Stern, R.J., 2005. Evidence from ophiolites, blueschists, and ultrahigh-pressure metamorphic terranes that the modern episode of subduction tectonics began in Neoproterozoic time. *Geology* 33, 557.
- Stixrude, L., de Koker, N., Sun, N., Mookherjee, M., Karki, B.B., 2009. Thermodynamics of silicate liquids in the deep Earth. *Earth and Planetary Science Letters* 278, 226–232.
- Sun, S.S., McDonough, W.F., 1989. Chemical and isotopic systematics of oceanic basalts: implications for mantle composition and processes. Geological Society, London, Special Publications 42, 313–345.
- Tackley, P.J., 2000. Self-consistent generation of tectonic plates in time-dependent, three-dimensional mantle convection simulations. *Geochemistry, Geophysics, Geosystems* 1.
- Tackley, P.J., 2008. Modelling compressible mantle convection with large viscosity contrasts in a three-dimensional spherical shell using the yin-yang grid. *Physics of the Earth and Planetary Interiors* 171, 7–18.
- Tackley, P.J., Ammann, M., Brodholt, J.P., Dobson, D.P., Valencia, D., 2013. Mantle dynamics in super-Earths: Post-perovskite rheology and self-regulation of viscosity. *Icarus* 225, 50–61.
- Tackley, P.J., King, S.D., 2003. Testing the tracer ratio method for modeling active compositional fields in mantle convection simulations. *Geochemistry, Geophysics, Geosystems* 4.
- Tang, M., Chen, K., Rudnick, R.L., 2016. Archean upper crust transition from mafic to felsic marks the onset of plate tectonics. *Science* 351, 372–375.
- Taylor, S.R., McLennan, S.M., 1985. *The continental crust: Its composition and evolution*. Blackwell Scientific Pub., Palo Alto, CA.
- Taylor, S.R., McLennan, S.M., 1996. The Evolution of Continental Crust. *Scientific American* 274, 76–81.
- van Thienen, P., van den Berg, A.P., Vlaar, N.J., 2004. On the formation of continental silicic melts in thermochemical mantle convection models: implications for early Earth. *Tectonophysics* 394, 111–124.
- Van Kranendonk, M.J., 2010. Two types of Archean continental crust: Plume and plate tectonics on early Earth. *American Journal of Science* 310, 1187–1209.
- Van Kranendonk, M.J., 2011. Cool greenstone drips and the role of partial convective overturn in Barberton greenstone belt evolution. *Journal of African Earth Sciences* 60, 346–352.
- Van Kranendonk, M.J., Collins, W.J., Hickman, A., Pawley, M.J., 2004. Critical tests of vertical vs. horizontal tectonic models for the Archean East Pilbara Granite–Greenstone Terrane, Pilbara Craton, Western Australia. *Precambrian Research* 131, 173–211.
- Van Kranendonk, M.J., Hugh Smithies, R., Hickman, A.H., Champion, D.C., 2007. Review: secular tectonic evolution of Archean continental crust: interplay between horizontal and vertical processes in the formation of the Pilbara Craton, Australia. *Terra Nova* 19, 1–38.
- Van Kranendonk, M.J., Kirkland, C.L., 2016. Conditioned duality of the Earth system: Geochemical tracing of the supercontinent cycle through Earth history. *Earth Science Reviews* 160, 171–187.
- Vogt, K., Gerya, T.V., Castro, A., 2012. Crustal growth at active continental margins: Numerical modeling. *Physics of the Earth and Planetary Interiors* 192–193, 1–20.
- Voice, P.J., Kowalewski, M., Eriksson, K.A., 2011. Quantifying the Timing and Rate of Crustal Evolution: Global Compilation of Radiometrically Dated Detrital Zircon Grains. *Journal of Geology* 119, 109–126.

- Wilde, S.A., Valley, J.W., Peck, W.H., Graham, C.M., 2001. Evidence from detrital zircons for the existence of continental crust and oceans on the Earth 4.4 Gyr ago. *Nature* 409, 175–178.
- Xie, S., Tackley, P.J., 2004a. Evolution of helium and argon isotopes in a convecting mantle. *Physics of the Earth and Planetary Interiors* 146, 417–439.
- Xie, S., Tackley, P.J., 2004b. Evolution of U-Pb and Sm-Nd systems in numerical models of mantle convection and plate tectonics. *Journal of Geophysical Research* 109.
- Xu, W., Lithgow-Bertelloni, C., Stixrude, L., Ritsema, J., 2008. The effect of bulk composition and temperature on mantle seismic structure. *Earth and Planetary Science Letters* 275, 70–79.
- Yamazaki, D., Karato, S.i., 2001. Some mineral physics constraints on the rheology and geothermal structure of Earth's lower mantle. *American Mineralogist* 86, 385–391.
- Zerr, A., Diegeler, A., Boehler, R., 1998. Solidus of Earth's deep mantle. *Science* 281, 243–246.
- Zhang, C., Holtz, F., Koepke, J., Wolff, P.E., Ma, C., Bédard, J.H., 2013. Constraints from experimental melting of amphibolite on the depth of formation of garnet-rich restites, and implications for models of Early Archean crustal growth. *Precambrian Research* 231, 206–217.